



**HAL**  
open science

## Embedded Coherent Structures from Magnetohydrodynamics to Sub-ion Scales in Turbulent Solar Wind at 0.17 au

Alexander Vinogradov, Olga Alexandrova, Pascal Démoulin, Anton Artemyev,  
Milan Maksimovic, André Mangeney, Alexei Vasiliev, Anatoli A. Petrukovich,  
Stuart Bale

► **To cite this version:**

Alexander Vinogradov, Olga Alexandrova, Pascal Démoulin, Anton Artemyev, Milan Maksimovic, et al.. Embedded Coherent Structures from Magnetohydrodynamics to Sub-ion Scales in Turbulent Solar Wind at 0.17 au. *The Astrophysical Journal*, 2024, 971, 10.3847/1538-4357/ad5288 . insu-04853427

**HAL Id: insu-04853427**

**<https://insu.hal.science/insu-04853427v1>**

Submitted on 23 Dec 2024

**HAL** is a multi-disciplinary open access archive for the deposit and dissemination of scientific research documents, whether they are published or not. The documents may come from teaching and research institutions in France or abroad, or from public or private research centers.








L'archive ouverte pluridisciplinaire **HAL**, est destinée au dépôt et à la diffusion de documents scientifiques de niveau recherche, publiés ou non, émanant des établissements d'enseignement et de recherche français ou étrangers, des laboratoires publics ou privés.



Distributed under a Creative Commons Attribution 4.0 International License



# Embedded Coherent Structures from Magnetohydrodynamics to Sub-ion Scales in Turbulent Solar Wind at 0.17 au

Alexander Vinogradov<sup>1,2</sup> , Olga Alexandrova<sup>1</sup> , Pascal Démoulin<sup>1</sup> , Anton Artemyev<sup>2,3</sup> , Milan Maksimovic<sup>1</sup> ,  
André Mangeney<sup>1</sup>, Alexei Vasiliev<sup>2</sup> , Anatoli A. Petrukovich<sup>2</sup>, and Stuart Bale<sup>4,5</sup> 

<sup>1</sup> LESIA, Observatoire de Paris, Université PSL, CNRS, Sorbonne Université, Université de Paris, 5 place Jules Janssen, 92195 Meudon, France; alexander.vinogradov@obspm.fr

<sup>2</sup> Space Research Institute of the Russian Academy of Sciences, Moscow, Russia

<sup>3</sup> Institute of Geophysics and Planetary Physics, University of California, Los Angeles, CA, USA

<sup>4</sup> Space Science Laboratory, University of California, Berkeley, CA, USA

<sup>5</sup> Physics Department, University of California, Berkeley, CA, USA

Received 2023 July 6; revised 2024 May 23; accepted 2024 May 29; published 2024 August 7

## Abstract

We study intermittent coherent structures in solar wind turbulence from MHD to kinetic plasma scales using Parker Solar Probe data during its first perihelion (at 0.17 au) in the highly Alfvénic slow solar wind. We detect coherent structures using Morlet wavelets. For the first time, we apply a multiscale analysis in physical space. At MHD scales within the inertial range, times scales  $\tau \in (1, 10^2)$  s, we find (i) current sheets including switchback boundaries and (ii) Alfvén vortices. Within these events are embedded structures at smaller scales: typically Alfvén vortices at ion scales,  $\tau \in (0.08, 1)$  s, and compressible vortices at sub-ion scales,  $\tau \in 8(10^{-3}, 10^{-2})$  s. The number of coherent structures grows toward smaller scales: we observe  $\sim 200$  events during a 5 hr time interval at MHD scales,  $\sim 10^3$  at ion scales, and  $\sim 10^4$  at sub-ion scales. In general, there are multiple structures of ion and sub-ion scales embedded within one MHD structure. There are also examples of ion and sub-ion scale structures outside MHD structures. To quantify the relative importance of different types of structures, we do a statistical comparison of the observed structures with the expectations of models of the current sheets and vortices. The results show the dominance of Alfvén vortices at all scales in contrast to the widespread view of the dominance of current sheets. This means that Alfvén vortices are important building blocks of Alfvénic solar wind turbulence.

*Unified Astronomy Thesaurus concepts:* Solar wind (1534); Space plasmas (1544); Interplanetary turbulence (830)

## 1. Introduction

Solar wind fluctuations cover a broad range of scales: from macroscopic scales, where the energy is injected into the MHD turbulent cascade, to microscales, where kinetic effects play an important role, and the energy is dissipated. The dissipation mechanism has not been understood yet. Numerical simulations indicate that dissipation occurs inhomogeneously (Wan et al. 2012; Karimabadi et al. 2013; Zhdankin et al. 2013; Kuzay et al. 2019). Regions of increased heating in the solar wind correlate with observations of coherent structures (Osman et al. 2011; Wu et al. 2013; Chasapis et al. 2015; Sioulas et al. 2022). Coherent structures can be defined as high-amplitude, stable, localized in space events with phase coherence over their spatial extent (Hussain 1986; Fiedler 1988; Veltri 1999; Bruno et al. 2001; Mangeney 2001; Farge & Schneider 2015; Alexandrova 2020).

Different types of coherent structures are observed in the solar wind at different scales. Large-scale flux tubes and flux ropes cover energy-containing scales and the inertial range (e.g., Moldwin et al. 2000; Borovsky 2008; Feng et al. 2008; Janvier et al. 2014; Zhao et al. 2020). Current sheets are usually observed at small scales of the inertial range and at ion scales (e.g., Siscoe et al. 1968; Burlaga 1969; Salem 2000; Knetter et al. 2004; Tsurutani et al. 2011; Lion et al. 2016; Perrone et al. 2016; Artemyev et al. 2019). Recent Solar Orbiter

observations reveal an embedded ion scale flux rope in a bifurcated current sheet (Eastwood et al. 2021). Alfvén vortices have been identified at MHD and ion scales (Verkhoglyadova et al. 2003; Lion et al. 2016; Perrone et al. 2016, 2017; Roberts et al. 2016). A recent numerical simulation shows that magnetic vortices emerge at the late stage of the reflection-driven turbulence (Meyrand et al. 2023). Compressible structures, such as magnetic holes (e.g., Turner et al. 1977; Stevens & Kasper 2007; Volwerk et al. 2020), solitons, and shocks (Salem 2000; Perrone et al. 2016), are observed at the end of the inertial range and at ion scales.

Coherent structures contribute significantly to the magnetic turbulent spectrum in the solar wind. Li et al. (2011) show that in the presence of current sheets, the inertial range spectrum is closer to the Kolmogorov scaling,  $-5/3$ , while without current sheets the spectrum is closer to the Iroshnikov–Kraichnan scaling,  $-3/2$ . In a case study of a fast wind stream by Lion et al. (2016), the contribution of coherent structures to the magnetic field spectrum is up to 40% from the inertial range down to ion scales. Therefore, coherent structures are energetically important elements of solar wind turbulence.

There are fewer observations of coherent structures on sub-ion scales. Cluster/STAFF allows the measure of sub-ion scale fluctuations at 1 au. Greco et al. (2016) studied ion scale current sheets and showed the presence of many smaller ones at sub-ion scales. In this study the authors used the partial variance of increments method (Greco et al. 2018), which is appropriate for detecting planar structures (e.g., see the discussion in Lion et al. 2016). Another study with Cluster, but applying Morlet wavelets, shows embedded Alfvén vortex-like fluctuations at



Original content from this work may be used under the terms of the [Creative Commons Attribution 4.0 licence](https://creativecommons.org/licenses/by/4.0/). Any further distribution of this work must maintain attribution to the author(s) and the title of the work, journal citation and DOI.

sub-ion scales in a current sheet at ion scales (Jovanović et al. 2018). To explain this observation, the authors developed the analytic model of a chain of Alfvén vortices embedded in the current sheet. At electron scales there are also signatures of Alfvén-vortex-like fluctuations detected by two Cluster satellites separated by 7 km only (Alexandrova 2020; Alexandrova et al. 2020).

The first multisatellite observations of these cylindrical structures in space plasma were obtained with the Cluster mission in the Earth’s magnetosheath behind a quasi-perpendicular bow shock (Alexandrova et al. 2006; Alexandrova 2008). Cassini measurements also indicate the presence of such structures in the Kronian magnetosheath (Alexandrova & Saur 2008). Signatures of Alfvén vortices in the solar wind using one satellite have been shown by Verkhoglyadova et al. (2003) and Lion et al. (2016). Roberts et al. (2016) and Perrone et al. (2016, 2017) confirmed the existence of Alfvén vortices in the solar wind with four satellites of Cluster. Wang et al. (2019) investigated the kinetic effects within an Alfvén vortex thanks to MMS measurements in the Earth’s magnetosheath.

In the present paper, we study magnetic turbulent fluctuations from MHD inertial range to sub-ion scales with Parker Solar Probe (PSP) data at 0.17 au. Using the Morlet wavelet transform, which is a good compromise between time and frequency resolution, we detect intermittent events that cover a wide range of scales. We show that these events correspond to embedded multiscale structures, from MHD to sub-ion scales. Then, we study in more detail the nature of these structures, which cover the whole turbulent cascade.

The article is organized as follows. Section 2 describes the PSP data used in the analysis. In Section 3 we identify MHD, ion and sub-ion ranges of scales based on the magnetic spectral properties and positions of ion characteristic scales in the spectrum. Section 4 is dedicated to the detection method of coherent structures. Section 5 presents several theoretical models of the structures we think we cross with PSP at different scales. Then, we study the sensitivity of minimum variance results for different spacecraft trajectories across the model structures for different noise levels. In Section 6 we describe a few examples of structures detected simultaneously at MHD, ion, and sub-ion scales. Section 7 describes the statistical study of the observed coherent events during 5 hr of the first PSP encounter at MHD, ion, and sub-ion scales. In Section 8 we summarize and discuss the results.

## 2. Data

We analyze a 5 hr time interval during the first perihelion, on 2018 November 6, [00:00, 05:00] UT, when the spacecraft at the distance of 0.17 au from the Sun measured the solar wind emerging from the small equatorial coronal hole (Bale et al. 2019; Kasper et al. 2019). The magnetic field during the chosen time interval is particularly highly disturbed due to the presence of high-amplitude structures (including switchbacks; Bale et al. 2019; Perrone et al. 2020). The duration of the chosen interval is long enough to resolve the inertial range of MHD turbulence, but not too long, so that the PSP is magnetically connected to the same coronal hole and the PSP position is nearly at the same radial distance from the Sun.

We use the merged magnetic field measurements of two magnetometers: FIELDS/Fluxgate Magnetometer and Search Coil (Bale et al. 2016; Bowen et al. 2020). These data have a 3.4 ms time resolution, which allows us to resolve a wide range

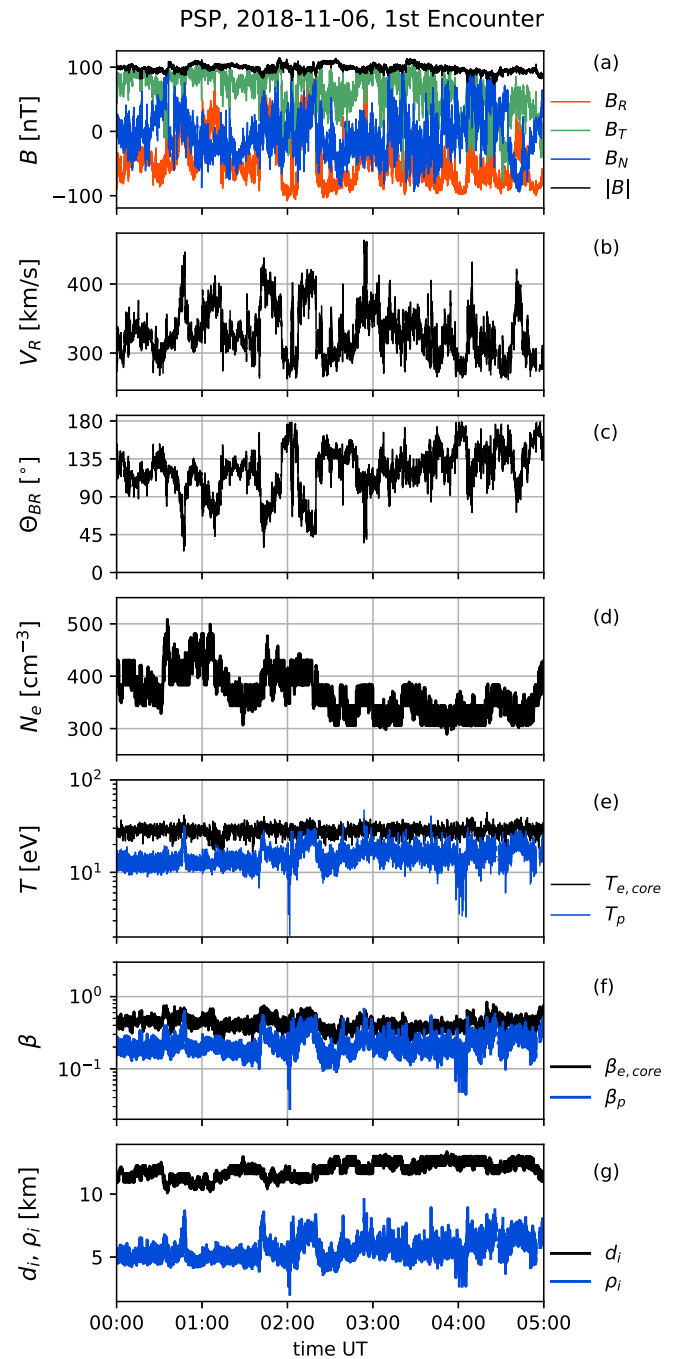


**Figure 1.** Overview of the solar wind data during the first perihelion of PSP at 0.17 au on 2018 November 6, between 00:00 and 05:00 UT. From top to bottom: (a) the magnetic field components in the RTN reference frame and the magnetic field modulus, (b) proton velocity radial component  $V_R$ , (c) angle between the magnetic field and the radial direction  $\Theta_{BR}$ , (d) electron density  $N_e$ , (e) proton temperature  $T_p$  (in blue) and core electron temperature  $T_{e,core}$  (in black), (f) core electron and proton plasma beta, (g) ion characteristic scales,  $d_i$  and  $\rho_i$ .

of scales, from the MHD inertial range to the sub-ion range. Due to the anomaly of the Search Coil at one of its axes (which happened in 2019 March), the full merged vector of the magnetic field is accessible only for the first perihelion (Bowen et al. 2020). Figure 1(a) shows the magnetic field magnitude  $B(t)$  in black and three components in the RTN coordinate frame in color. The magnetic field vector fluctuates around  $\langle \mathbf{B} \rangle = (-47, 63, -5)$  nT. Its magnitude is nearly constant  $|\mathbf{B}| = 98 \pm 5$  nT. The angle

between the magnetic field and the radial direction changes from  $25^\circ$  to  $180^\circ$  as shown in Figure 1(c), with a dominance around quasi-perpendicular orientation,  $\langle\Theta_{BR}\rangle = 121^\circ$  with standard deviation  $\sigma(\Theta_{BR}) = 26^\circ$ .

To characterize plasma bulk velocity, we use the SWEAP/SPC Faraday cup instrument (Kasper et al. 2016). Proton velocity  $V$  is estimated from the first moment of the distribution function. Figure 1(b) shows its radial component  $V_R$ . The mean velocity is  $\langle V \rangle = (330, 70, 8) \text{ km s}^{-1}$ , making a nonzero angle with the radial direction:  $\langle\Theta_{VR}\rangle = 14^\circ$ . This small deviation from the radial of the solar wind speed might not be accurate due to the field of view of the instrument together with the high angular satellite velocity during the considered time interval (Michael Stevens, 2024, private communication). It may introduces a relative error of about 3% on the estimates of spatial scales  $\ell$  using the Taylor hypothesis.

We use RFS/FIELDS quasi-thermal noise (QTN) electron plasma data to characterize electron plasma parameters (Moncuquet et al. 2020). Electron density  $N_e$  is determined from the electrostatic fluctuations at the electron plasma frequency, and it is shown in Figure 1(d).

Proton temperature  $T_p$  is estimated from the second moment of the distribution function measured by the SWEAP/SPC instrument. Figure 1(e) shows QTN electron core temperature  $T_{e,\text{core}}$  (in black) and proton temperature  $T_p$  (in blue). The mean temperatures are  $\langle T_{e,\text{core}} \rangle = 28.5 \text{ eV}$  and  $\langle T_p \rangle = 15 \text{ eV}$ .

We consider solar wind fluctuations over a wide range of timescales. The minimum timescale is determined by the temporal resolution of the magnetic data  $dt = 3.4 \times 10^{-3} \text{ s}$  and the maximum by the total duration of the time interval  $T = 5 \text{ hr}$ . The spatial scales of the corresponding range, estimated using the Taylor hypothesis with  $V = 340 \text{ km s}^{-1}$ ,  $\ell \in [1, 10^5] \text{ km}$ , are much larger than the Debye length,  $\lambda_D \simeq 2 \text{ m}$ ; therefore the plasma is quasi-neutral. During the analyzed time period, alpha particle abundance has not been measured, but it can be estimated as  $A_\alpha = N_\alpha/N_p < 5\%$  (Kasper et al. 2007; Alterman & Kasper 2019; Liu et al. 2021). The QTN spectroscopy provides a more accurate measurement of the density than particle detectors, so we use  $N_p = N_e$  and calculate proton plasma beta  $\beta_p$  using the electron density:  $\beta_p = N_e k T_p / (B^2 / 2\mu_0)$ , with  $\mu_0$  being the magnetic permeability. Plasma beta for core electrons is defined as  $\beta_{e,\text{core}} = N_e k T_{e,\text{core}} / (B^2 / 2\mu_0)$ . Both plasma  $\beta$  parameters are well below unity as shown in Figure 1(f),  $\langle\beta_p\rangle = 0.22$  and  $\langle\beta_{e,\text{core}}\rangle = 0.44$ . Figure 1(g) shows the time variation of the ion characteristic spatial scales  $d_i = c/\omega_{pi}$ , where  $\omega_{pi} = \sqrt{4\pi N_p e^2/m_p}$  and  $\rho_i = V_{\text{th},\perp}/\omega_{ci}$ , where  $V_{\text{th},\perp} = \sqrt{2k_B T_\perp/m_p}$  is the perpendicular proton thermal speed and  $\omega_{ci} = eB/m_p c$  is the proton gyrofrequency.

### 3. MHD, Ion, and Sub-ion Range Identification

First, we describe the magnetic field spectral properties of the analyzed time interval. We apply a wavelet transform with a Morlet mother function (Torrence & Compo 1998):

$$\psi_0(t) = \pi^{-1/4} e^{-t^2/2} e^{i\omega_0 t}, \quad (1)$$

where  $\omega_0 = 6$  is the angular frequency of oscillations in the mother function (with normalized time). The wavelet transform of the magnetic field component  $B_i(t)$  is defined as the convolution of  $B_i(t)$  with scaled, translated, and normalized

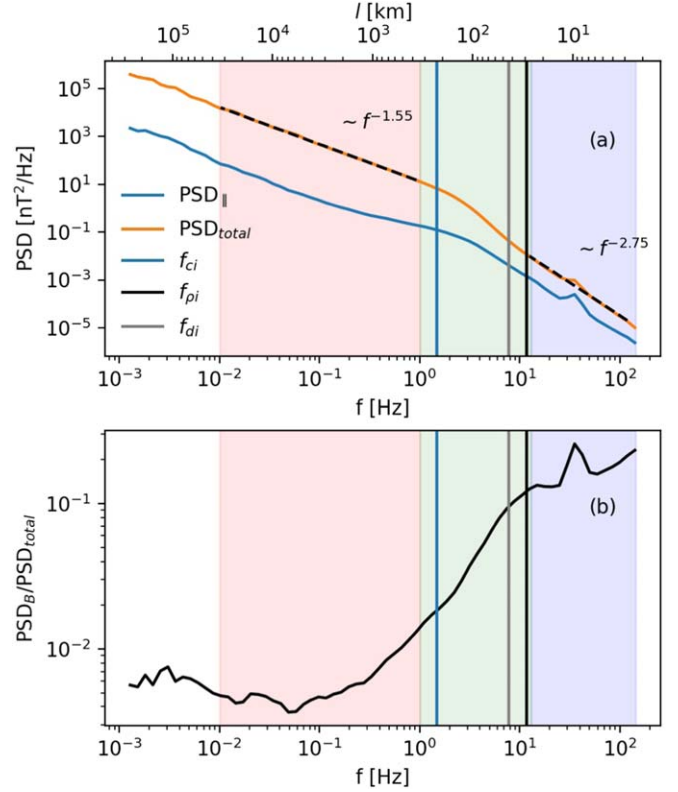


**Figure 2.** (a) Magnetic field total spectrum  $S_{\text{total}}$  in orange and magnetic field modulus spectrum that is the proxy of the parallel fluctuations spectrum  $S_{\parallel}$  (Equation (5)), and (b) the ratio  $S_{\parallel}/S_{\text{total}}$ . The vertical lines show the characteristic ion scales: ion cyclotron frequency  $f_{ci}$  (in blue), the frequencies computed with the Doppler-shifted ion gyroradius  $f_{pi}$  (in black), and the Doppler-shifted ion inertial length  $f_{di}$  (in gray). The frequency ranges are highlighted: MHD in red, ion scales in green, and sub-ion scales in blue.

$\psi_0(t)$  to have a mother function  $\psi$  with unit energy:

$$W[B_i](t, \tau) = \sum_{n'=0}^{N-1} B_i(t') \psi^*[(t' - t)/\tau] \quad (2)$$

where the sign \* indicates the complex conjugate.

Wavelet coefficients are influenced by the edge effects. The cone of influence (COI) curve separates the region of scales where edge effects become important as a function of time. To avoid this edge effect we consider a maximum scale equal to  $\tau_{\text{max}} = 10^3 \text{ s}$ . The intercept of  $\tau_{\text{max}}$  with the COI curve determines the time subinterval  $T' = [00:22:49, 04:37:11] \text{ UT}$  where wavelet coefficients at the scales  $\tau < \tau_{\text{max}}$  are not influenced by the edge effect.

Figure 2(a), orange line, shows the total magnetic field power spectral density (PSD)  $S_{\text{total}}(\tau)$ , calculated using the time-averaging over the subinterval  $T'$ :

$$S_{\text{total}}(\tau) = \frac{2\delta t^2}{T'} \sum_{i \in T'} \sum_{i=R,T,N} |W[B_i](t, \tau)|^2, \quad (3)$$

where  $\delta t = 0.008 \text{ s}$  is the time step of the PSP merged magnetic field data. The relation between Fourier frequencies  $f$  and timescales  $\tau$  is  $f \simeq 1/\tau$  for the Morlet wavelets with  $\omega_0 = 6$ . In Figure 2(a), the blue line shows the PSD of compressive magnetic fluctuations. Compressive fluctuations are approximated here by the variation of magnetic field modulus. Indeed, this approximation is valid if the level of the fluctuations is

significantly lower than the mean field  $B_0$ , i.e.,  $\delta B/B_0 \ll 1$  (Perrone et al. 2016):

$$\delta(|B|^2) = |\mathbf{B}_0 + \delta\mathbf{B}|^2 - |\mathbf{B}_0|^2 \approx 2\delta B_{\parallel} B_0 \approx \delta(B_{\parallel}^2). \quad (4)$$

In the inertial range and at higher frequencies the condition  $\delta B/B_0 \ll 1$  is valid. So we calculate the parallel PSD,  $S_{\parallel}(\tau)$ , as was done by Perrone et al. (2016):

$$S_{\parallel}(\tau) = \frac{2\delta t^2}{T'} \sum_{t \in T'} |W[|B_{\parallel}|](t, \tau)|^2. \quad (5)$$

As we can see from Figure 2(a),  $S_{\text{total}}(f) \sim f^{-1.55}$  within the inertial range  $10^{-2} < f < 1$  Hz, in agreement with Chen et al. (2020). Approaching ion kinetic scales, the spectrum steepens. The ion transition range, or simply ion scales, is present where the spectrum changes continuously its slope (Alexandrova et al. 2013; Kiyani et al. 2015). It is observed here nearly between the ion cyclotron frequency  $f_{ci} = eB/2\pi m_i = 1.4$  Hz and the frequency of the Doppler-shifted ion gyroradius  $f_{\rho i} = V/2\pi \rho_i = 11.4$  Hz. The frequency of the Doppler-shifted ion inertial length  $f_{di} = V/2\pi d_i$  is in between these two frequencies. At  $f > 13$  Hz (sub-ion scales), the spectral index stabilizes at  $-2.75$ , in agreement with what is observed at 0.3 and 1 au between ion and electron scales (Alexandrova et al. 2009, 2012, 2021; Chen et al. 2010).

Based on the magnetic field spectral properties and characteristic plasma scales ( $f_{ci}$ ,  $f_{\rho i}$ , and  $f_{di}$ ) we define the following frequency ranges  $\Delta f_j$ , shown as transparent color bands in Figure 2:

$$\Delta f_j = \begin{cases} (10^{-2}, 1) \text{ Hz} & \text{MHD inertial range (in red)} \\ (1, 13) \text{ Hz} & \text{ion scales (in green)} \\ (13, 128) \text{ Hz} & \text{sub-ion range (in blue)}. \end{cases} \quad (6)$$

The corresponding timescale ranges  $\tau_j$  will be used later in this article, and the index  $j$  here and further in the article refers to one the following ranges:

$$\tau_j: \begin{cases} \tau_{\text{MHD}} = (1, 100) \text{ s} \\ \tau_{\text{ion}} = (0.08, 1) \text{ s} \\ \tau_{\text{subion}} = (0.008, 0.08) \text{ s}. \end{cases} \quad (7)$$

The ratio of compressible fluctuations to the total PSD  $S_{\parallel}/S_{\text{total}}$  is shown in Figure 2(b). In the inertial range, parallel magnetic fluctuations are much less energetic than perpendicular ones ( $\delta B_{\parallel} \ll \delta B_{\perp}$ ), as is usually observed in the solar wind. At the sub-ion scales, the fraction of the parallel  $S_{\parallel}(\tau)/S_{\text{total}}(\tau)$  increases up to  $\simeq 0.2$ , which is consistent with the results of Salem et al. (2012) at 1 au. The authors suggested that the observed spectral ratio can be explained by the presence of the kinetic Alfvén wave (KAW) cascade with nearly perpendicular wavevectors ( $k_{\perp} \gg k_{\parallel}$ ). However, analyzing Cluster measurements (Lacombe et al. 2017) and a 2D hybrid numerical simulation (Matteini et al. 2020) found that the asymptotic compressibility value at sub-ion scales does not match perfectly the KAW prediction. Finally, recent numerical simulations indicate that coherent structures, rather than waves, are energetically dominant on sub-ion scales (Papini et al. 2021).

#### 4. Detection of Coherent Structures from MHD to Sub-ion Scales

In this section, we describe the methodology to detect the structures from MHD down to sub-ion scales.

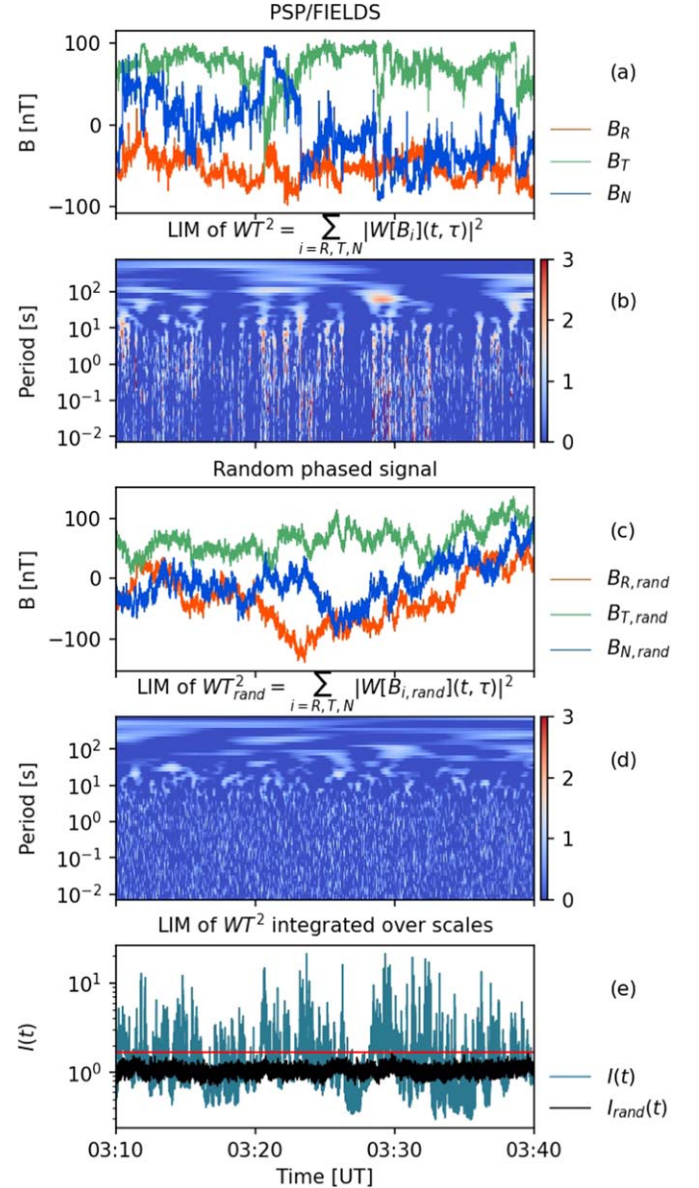


**Figure 3.** A 30 minutes zoom, [03:10, 03:40] UT, within the analyzed time interval of 5 hr on 2018 November 6. From top to bottom: (a) magnetic field in the RTN reference frame; (b) LIM of the magnetic fluctuations of the total energy  $L(t, \tau)$ , Equation (8); (c) artificial magnetic field  $\mathbf{B}_{\text{rand}}$  with random phases and the same Fourier amplitudes as original magnetic field measurements; (d) LIM of the artificial signal  $L_{\text{rand}}(t, \tau)$ ; (e) the comparison of the integrated LIMs  $I(t) = \langle L(t, \tau) \rangle_{\tau \in [10^{-2}, 10^3] \text{ s}}$  (blue) and the  $I_{\text{rand}}(t) = \langle L_{\text{rand}}(t, \tau) \rangle_{\tau \in [10^{-2}, 10^3] \text{ s}}$  (black). The horizontal red line shows  $I_{\text{threshold}} = \max(I_{\text{rand}}(t))$  as defined in Figure 4.

##### 4.1. Local Intermittency Measure

We use the Local Intermittency Measure (LIM)  $L(t, \tau)$ ; (Farge 1992) based on Morlet wavelets to detect the structures. The value  $L(t, \tau)$  shows the total energy of fluctuations at a given moment in time  $t$  at a given timescale  $\tau$ , relative to the average energy at that scale:

$$L(t, \tau) = \frac{\sum_{i=R,T,N} |W[B_i](t, \tau)|^2}{\langle \sum_{i=R,T,N} |W[B_i](t, \tau)|^2 \rangle_{t \in T'}} \quad (8)$$

where  $T'$  is the analyzed time interval.

In Figure 3 we show a 30 minutes zoom within  $T'$ . Panel (a) gives RTN components of the measured  $\mathbf{B}$ . Panel (b) shows the

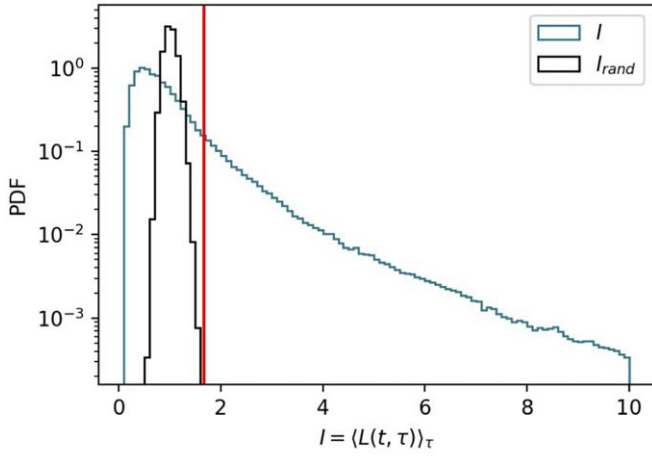


**Figure 4.** Histograms of the integrated LIM  $I(t)$  and the random-phased integrated LIM  $I_{\text{rand}}(t)$ . The threshold  $I_{\text{threshold}} = \max(I_{\text{rand}}(t))$  is shown by the red vertical line.

observed  $L(t, \tau)$ . The vertical elongations of enhanced  $L(t, \tau)$  values are due to coupled (or coherent) phases of the fluctuations (Lion et al. 2016; Perrone et al. 2016; Alexandrova 2020). Indeed, to see this point better, we construct an artificial signal that has the same Fourier spectrum as the original magnetic field measurements, but with random phases (Hada et al. 2003; Koga & Hada 2003). This synthetic signal  $\mathbf{B}_{\text{rand}}$  is shown in Figure 3(c), while the corresponding LIM  $L_{\text{rand}}(t, \tau)$  is shown in panel (d). The energy distribution of the synthetic signal is incoherent (randomly distributed in the  $(t, \tau)$  plane); i.e., peaks of  $L_{\text{rand}}(t, \tau)$  at different  $\tau$  are not observed at the same time. Therefore, the vertical elongations in the observed  $L(t, \tau)$  correspond to magnetic fluctuations with coupled phases across scales where the elongation is observed. The high energy of these events with respect to the mean is a sign of intense coherent structures formed in the turbulent medium (e.g., Farge 1992; Bruno 2019). So, we observe coherent structures that extend from inertial to sub-ion timescales. Using the Taylor hypothesis, the timescale range  $\tau \in \tau_{\text{all}} = [10^{-2}, 10^3]$  s can be converted into the spatial range  $\ell = V \cdot \tau \in [3, 3 \times 10^3]$  km, or  $\ell/\rho_i = 6[0.1, 10^4]$  in terms of the ion Larmor radius ( $\rho_i = 5$  km).

The difference between random-phased signal and original magnetic field data suggests a methodology for detecting the central times of coherent structures. Specifically, we sum the LIM over the timescale range  $\tau_{\text{all}} = [10^{-2}, 10^3]$  s, where wavelet timescales  $\tau$  are logarithmically spaced with the base 2; see Equation (9) in Torrence & Compo (1998):

$$I(t) = \sum_{\tau \in \tau_{\text{all}}} L(t, \tau). \quad (9)$$

Figure 3(e) shows  $I(t)$ ; (blue line), random-phased integrated LIM  $I_{\text{rand}}(t)$ ; (black line) and the threshold  $I_{\text{threshold}} = \max(I_{\text{rand}}(t))$ ; (red horizontal line). The local maxima of  $I(t) > I_{\text{threshold}}$  gives the central times of the coherent structures present in the original signal. In the following, we refer to this method as *the integrated LIM selection*.

The comparison of original  $I(t)$  and random-phased  $I_{\text{rand}}(t)$  distributions is shown in Figure 4. The  $I_{\text{rand}}$  distribution (in black) is close to Gaussian with a mean of 1 (because of the normalization and random phases). On the contrary,  $I(t)$ ; (in

blue-azure) has a long tail of extreme values due to the presence of coherent structures integrated over all timescales.

The integrated LIM selection does not have a predetermined scale at which the structure is searched for but it is preferentially focused on scales where the vertical enhancements in the LIM  $L(t, \tau)$  are observed. Applying it on  $T' = [00:22:49, 04:37:11]$  on 2018 November 6, we find  $N = 9485$  structures. If we define the filling factor of the structures as the normalized total time duration where the integrated LIM is over the threshold:

$$P = \text{Time}(I(t) > I_{\text{threshold}})/T', \quad (10)$$

we find that the structures cover 14% of the analyzed time interval  $T'$ .

In this paper, we will also use the integrated LIM over the reduced timescale ranges to understand in more detail the nature of the structures at MHD, ion, and sub-ion scales, where physics is different. So, we can define integrated LIM  $I_i = (I_{\text{MHD}}, I_{\text{ion}}, I_{\text{subion}})$  over the corresponding range of timescales  $\tau_j = (\tau_{\text{MHD}}, \tau_{\text{ion}}, \tau_{\text{subion}})$ , defined in Equation (6):

$$I_j(t) = \sum_{\tau \in \tau_j} L(t, \tau). \quad (11)$$

Similarly, integrating  $L_{\text{rand}}(t, \tau)$  over  $\tau_j$  we define random-phased integrated LIM  $I_{\text{rand},j}(t)$ . Thus, we can find the central times of the structures within these scale bands as the times of the local maxima for  $I_j(t) > I_{\text{threshold},j} = \max(I_{\text{rand},j}(t))$ .

This band-integrated LIM selection allows us to see how the number of the structures and filling factor changes with the band of scales.

In order to count isolated coherent structures, we find continuous time intervals when  $I_j(t) > I_{\text{threshold},j}$ .  $N_j$  denotes the number of isolated events at each range of scales. We define the filling factor  $P_j$  as follows

$$P_j = \text{Time}(I_j(t) > I_{\text{threshold},j})/T'.$$

We find a relatively small number of MHD scale structures ( $N_{\text{MHD}} = 196$ ) with high filling factor ( $P_{\text{MHD}} = 12\%$ ), compared to  $P_{\text{ion}} = 7\%$  and  $P_{\text{sub-ion}} = 6\%$  for much more numerous ion scale structures ( $N_{\text{ion}} = 2028$ ) and sub-ion scale structures ( $N_{\text{sub-ion}} = 11,167$ ). We remark that our estimations of  $P$  are conservative, as far as only time where LIM is over the threshold is counted, but the structure's field decreasing from its center exists outside of the time where the energy of the structure is concentrated, e.g., Perrone et al. (2016). So, the filling factor can be more than twice as large as indicated herein. Finally, numerous small-scale events populate larger ones and may exist outside them as well.

## 4.2. Magnetic Field at Different Scales

Thanks to Morlet wavelets and LIM we know now the central times of the structures covering all scales and the ones within different scale bands. In order to study magnetic field fluctuations  $\delta\mathbf{B}$  in the physical space around these central times, within different scale bands, we use a bandpass filter for fluctuations on frequency ranges given by Equation (6) and shown by color bands in Figure 2. We complete this analysis by studying the large-scale fluctuations of  $\mathbf{B}_{\text{lowpass}} - \mathbf{B}_0$  where the mean field  $\mathbf{B}_0$  is defined as the average field over the time interval  $T'$ . We use a finite impulse response (FIR) Hamming low-pass filter with a

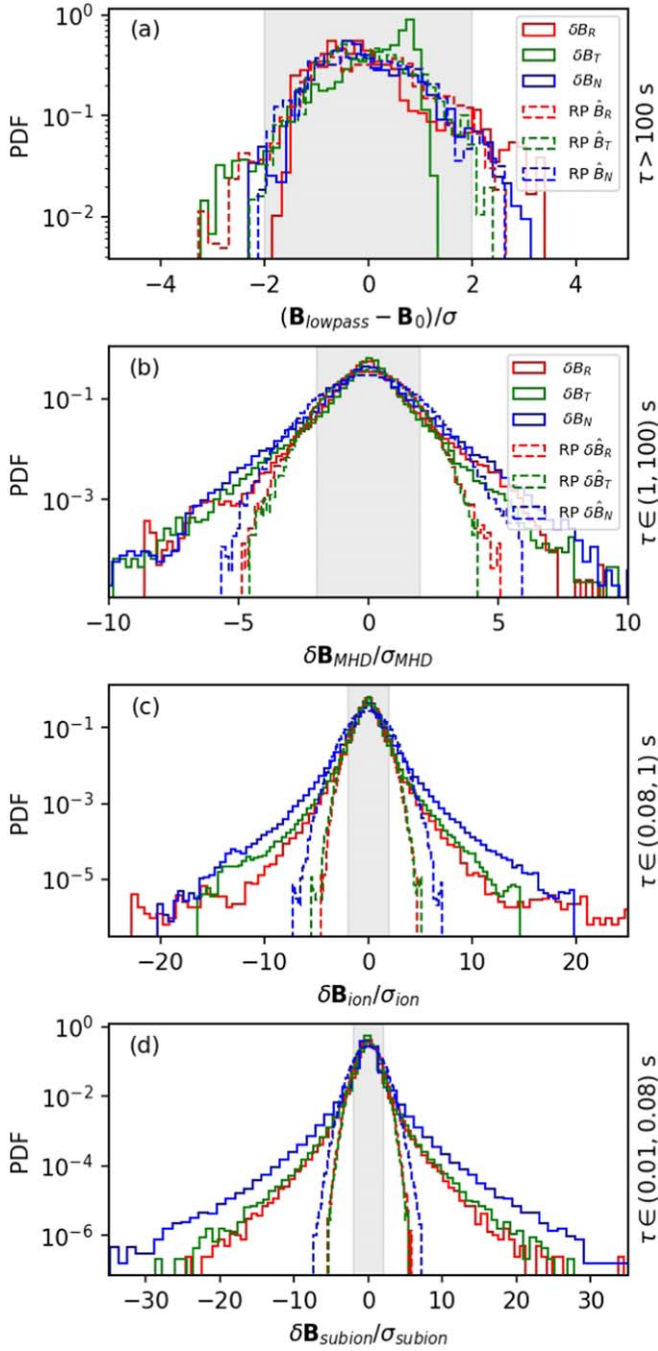


**Figure 5.** Histograms of magnetic field fluctuations (solid) compared to the signal with random phases (RP, dashed). The first panel from the top shows the centered low-pass-filtered fluctuations of the magnetic field. Panels (b)–(d) show bandpass-filtered fluctuations on MHD inertial, ion kinetic, and sub-ion scales, respectively. The horizontal axis is normalized to the standard deviation of the random-phased signal. The area within two standard deviations of the random-phased signal is highlighted in gray.

cutoff frequency of  $10^{-2}$  Hz to calculate the large-scale magnetic field fluctuations of  $\delta\mathbf{B} = \mathbf{B}_{\text{lowpass}} - \mathbf{B}_0$  (Smith 1997).

Figure 5 shows distributions of the filtered magnetic field (solid lines) compared to the filtered signal with random phases (dashed lines). Panel (a) shows the low-pass-filtered fluctuations of the magnetic field. Panels (b)–(d) show the FIR Hamming bandpass-filtered fluctuations on MHD, ion, and sub-ion scales, respectively. At each band of scales, we characterize

the amplitude of incoherent fluctuations as follows:

$$\sigma_{\text{noise},j} = \text{std}(\delta\mathbf{B}_j(t \in T_{\text{no struct}})) \quad (12)$$

where  $T_{\text{no struct}} = \text{Time}(I_j(t) < I_{\text{threshold},j})$ . The gray area in panels (b)–(d) is bounded by  $\delta\mathbf{B}_{\text{rand},j}/\sigma_{\text{noise},j} = \pm 2$ .

The random-phased signal fluctuations have Gaussian distributions at all scales (Figure 5). The observed  $\delta\mathbf{B}$  show scale-dependent deviations from Gaussianity. Table 1 gives the moments of the observed distributions for three components at four different scale ranges. The distributions have nonzero skewness  $s$  (a normalized measure of a distribution asymmetry). The fourth normalized moment, kurtosis  $\kappa$ , increases from 3 to 4 at large scales, up to 12–24 at sub-ion scales. In comparison, Gaussian noise has  $s = 0$  and  $\kappa = 3$ .

Distributions of low-pass magnetic field components are asymmetric with respect to zero, especially radial and tangential (see Figure 5(a)). The skewness of those components has high absolute value and opposite signs:  $s_R = 1.1$  and  $s_T = -1.1$ . The low-pass magnetic field distributions do not have pronounced non-Gaussian tails, so the kurtosis  $\kappa$  is slightly above 3, and so close to the Gaussian noise value (see Table 1).

In the inertial and smaller-scale ranges, the distributions have weaker asymmetry ( $\langle |s| \rangle = (|s_R| + |s_T| + |s_N|)/3 \leq 0.2$ ). Non-Gaussian tails are identified at MHD scales (Figure 5(b)) and become even more pronounced at ion and sub-ion scales (Figures 5(c)–(d)). The kurtosis  $\kappa_T$  and  $\kappa_N$  monotonically increase from MHD to sub-ion scales (see Table 1). The kurtosis of the radial magnetic field  $\kappa_R$  component is growing from MHD to ion scales and then decreases at sub-ion scales. This behavior of  $\kappa_R$  can be explained by the proximity of the SCM noise, which starts to influence  $\delta B_{R,\text{subion}}$ , the weakest of the three components of magnetic fluctuations at these scales; see the red probability distribution function in Figure 5(d).

## 5. Model Structures

In this section, we discuss several models of the coherent structures. This gives us a necessary background to determine the dominant type of structures in the large statistics of events. These models have been developed in the MHD framework. Therefore, they are not applicable a priori for ion and sub-ion scales. But kinetic-scale turbulence may be described with fluid-like equations, which are structurally similar to reduced MHD equations. Therefore, it is reasonable to expect that similar types of structures (vortices, current sheets) can be distinguished among coherent structures on ion and sub-ion scales. This is why we compare these models of coherent structures at kinetic scales, as well.

The trajectory of a spacecraft across a structure matters for the polarization and the amplitude anisotropy of magnetic fluctuations. That is why we will explore the polarization and the Minimum Variance Analysis (MVA; Sonnerup & Scheible 1998) results as a function of the spacecraft trajectory across the model structures.

### 5.1. Alfvén Vortices

Alfvén vortices are cylindrically symmetric coherent structures that were introduced by Petviashvili & Pokhotelov (1992). Within these vortices, the generalized Alfvén relation  $\delta V_{\perp}/V_A = \xi \delta\mathbf{B}_{\perp}/B_0$  is verified, with  $\xi$ , which may be different from 1.

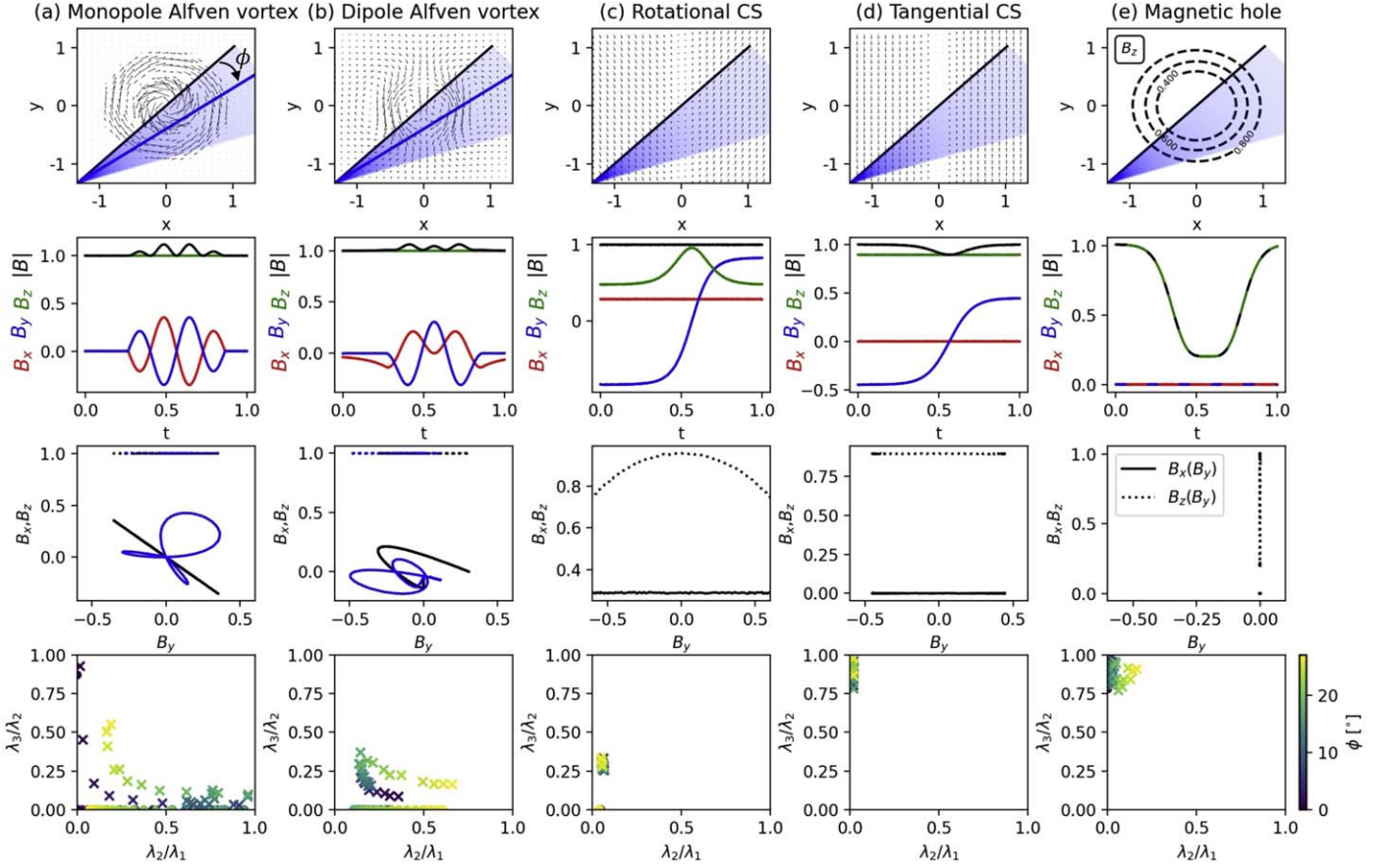


**Figure 6.** Simulation of the spacecraft crossing (a) a monopole Alfvén vortex, (b) a dipole vortex, (c) a rotational and (d) a tangential discontinuity, and (e) a magnetic hole. The first row shows the magnetic field vector in the plane perpendicular to the background magnetic field. The sector, shown in blue, is a set of trajectories crossing the structure at different angles in order to collect statistics of MVA eigenvalues. The panels in the second line show the magnetic field in the MVA frame of reference, which would be measured by the spacecraft when it crosses the structure along the black trajectory. Panels in the third line show the hodograph—indicating polarization for off-center (blue) and central (black) trajectories. The bottom row shows the eigenvalue ratios for the set of trajectories shown within the blue cone in the first row in the presence of noise, with  $\epsilon = 0.001$  (circles) and  $\epsilon = 0.1$  (crosses), where  $\epsilon$  is defined in Equation (15). The trajectory angle  $\phi$ , defined in the top-left panel, is coded with colors (see the color scale at the right bottom).

**Table 1**  
Main Parameters of the Distributions Shown in Figure 5 for the Magnetic Field Components

Filtering	$\sigma_R$	$\sigma_T$	$\sigma_N$	$\sigma_{\text{noise}}$	$s_R$	$s_T$	$s_N$	$\langle  s  \rangle$	$\kappa_R$	$\kappa_T$	$\kappa_N$	$\langle \kappa \rangle$
Low-pass	37	31	35	...	1.1	-1.1	0.5	0.9	3.8	3.8	3.1	3.6
MHD	9	8.6	11	7.8	0.2	-0.5	0.01	0.2	7.7	8.7	6.5	7.6
Ion scales	1.5	1.6	2.2	1.55	0.1	-0.2	-0.01	0.1	16.3	14.0	10.8	13
Sub-ion	0.12	0.12	0.15	0.11	0.01	-0.01	-0.04	0.02	11.6	19.3	24.4	18

**Note.** From left to right: standard deviation  $\sigma_{RTN}$  [nT], average standard deviation  $\sigma_{\text{noise}}$  [nT] (in absence of coherent structures), skewness  $s_{RTN}$ , average absolute skewness  $\langle |s| \rangle$ , kurtosis  $\kappa_{RTN}$ , and the average kurtosis  $\langle \kappa \rangle$ .

### 5.1.1. Monopole Alfvén Vortex

Figure 6 (column (a), top row) shows the crossing of a monopole vortex (Petviashvili & Pokhotelov 1992); details of the model are described in Appendix A.1.1. The set of trajectories, selected to cross the vortex, is shown by the blue transparent cone on the top-left panel of Figure 6. The set is parameterized by the angle  $\phi$ . Two trajectories, central ( $\phi = 0^\circ$ ) and off-center ( $\phi = 10^\circ$ ), are shown in black and blue lines correspondingly. The second panel from the top shows the three magnetic field components of the monopolar vortex crossed by a spacecraft along the black trajectory in the top panel. The third panel shows the dependencies  $B_x(B_y)$  and

$B_z(B_y)$  for both central and off-center trajectories (black and blue lines, respectively). The off-center trajectory has “clover”-like polarization in  $B_x(B_y)$ ; (blue curve). In the case of the crossing through the center, the polarization is linear (black line).

Figure 6 (column (a), bottom row) shows the MVA eigenvalue ratio  $\lambda_3/\lambda_2$  as a function of  $\lambda_2/\lambda_1$  for 50 different trajectories (see the blue cone in the top panel). The eigenvalues are ordered as  $\lambda_1 \geq \lambda_2 \geq \lambda_3$ , with the eigenvector  $\mathbf{e}_3$  being the minimum variance direction. The color between violet and yellow indicates the angle  $\phi$  of the trajectories:  $\phi = 0^\circ$  corresponds to the crossing through the center and  $\phi = 25^\circ$  corresponds to the side crossing.



In this plot, we test the effect of added noise with a relative amplitude  $\epsilon$  defined by

$$\epsilon = \delta B_{\text{noise}} / \delta B_{\perp} \quad (13)$$

where  $\delta B_{\text{noise}}$  is the noise amplitude and  $\delta B_{\perp}$  is the amplitude of the vortex. The eigenvalue ratios  $\lambda_2/\lambda_1$  and  $\lambda_3/\lambda_2$  are dependent on  $\epsilon$ . The results for two levels of noise are shown:  $\epsilon_1 = 0.001$  with filled circles, and  $\epsilon_2 = 0.1$  with crosses. In the case of negligible noise, the points are located along the  $x$ -axis (see circles). For larger  $\epsilon$ , the eigenvalues become more comparable, and the plane  $(\lambda_2/\lambda_1, \lambda_3/\lambda_2)$  fills up: the data form the *shape of a croissant* (see crosses). In the case of very large noise (and in the case of random fluctuations), the eigenvalues become of the same order, i.e.,  $\lambda_2/\lambda_1 \sim \lambda_3/\lambda_2 \sim 1$  (not shown). In Section 7,  $\epsilon$  is estimated from observations.

For the majority of trajectories, except central ( $\phi < 3^\circ$ ) and extreme off-center/tangential ones ( $\phi > 22^\circ$ ), the minimum variance direction  $\mathbf{e}_3$  is well defined ( $\lambda_3/\lambda_2 \sim 0$ ) and it is parallel to the axis of the vortex. Indeed, the vortex model describes  $\delta B_{\perp}$  and assumes  $\delta B_z = 0$ . So, in observations,  $\mathbf{e}_3$  (when it is well defined) is a good approximation for the vortex axis. So far as the vortex cylinder is field aligned, the angle between  $\mathbf{e}_3$  and  $\mathbf{B}_0$  must be small,  $\theta_{B_0,3} \sim 0^\circ$ .

In the case of the central crossing ( $\phi < 3^\circ$ ), only  $\mathbf{e}_1$  is well defined, because  $\lambda_2/\lambda_1 \sim 0$ ,  $\lambda_3/\lambda_2 \sim 1$ . In this case, the eigenvector of maximal variance  $\mathbf{e}_1$  is perpendicular to the crossing trajectory ( $\mathbf{e}_1 \perp \mathbf{V}$ ) and to the background magnetic field ( $\mathbf{e}_1 \perp \mathbf{B}_0$ ). Therefore,  $\theta_{V,1} \sim 90^\circ$  and  $\theta_{B,1} \sim 90^\circ$  are expected in observations.

In addition, for the vortex to be observable, the spacecraft must cross it along a trajectory inclined at a sufficient angle relative to the vortex axis, so  $\theta_{BV} \neq 0^\circ$  and  $\theta_{V,3} \neq 0^\circ$  (if  $\mathbf{e}_3$  is well defined).

### 5.1.2. Dipole Alfvén Vortex

In Figure 6 column (b), the top panel shows the magnetic field of the dipole vortex. This type of Alfvén vortices is particular, because its axis is inclined with respect to the background magnetic field and it is propagating; see details of the model in Appendix A.1.2. The magnetic field components are symmetric in time around the vortex axis (while for the monopole vortex they are antisymmetric). The magnetic polarization (third panel from the top) is different for the crossing at the vortex center (black trajectory) and the side crossing (blue trajectory).

Figure 6 (column (b), bottom panel) gives the minimal variance eigenvalues ratios for two noise levels. In the case of the low noise,  $\epsilon = 0.001$ ,  $\lambda_3/\lambda_2 \sim 0$ , and  $\lambda_2/\lambda_1 \in [0.1, 0.6]$  (filled circles). For  $\epsilon = 0.1$ , as for the monopole vortex, both ratios increase: the points in the  $(\lambda_2/\lambda_1, \lambda_3/\lambda_2)$  plane move toward the upper-right corner.

The magnetic fluctuations of the dipole vortex are transverse, so the minimum variance direction  $\mathbf{e}_3$  (when it is well defined) is along the axis of the vortex. The angle between  $\mathbf{e}_3$  and  $\mathbf{B}_0$  is expected to be small  $\theta_{B_0,3} \sim 0^\circ$  according to the assumption of the model. Maximum and intermediate MVA eigenvectors  $\mathbf{e}_1$ ,  $\mathbf{e}_2$  lie in the plane perpendicular to  $\mathbf{B}_0$ .

## 5.2. Current Sheets

Current sheets are planar coherent structures that separate the plasma with different magnetic field directions. MHD classification of current sheets includes rotational and tangential discontinuities (RDs and TDs, respectively; e.g., Baumjohann & Treumann 1997; Tsurutani et al. 2011).

### 5.2.1. Rotational Discontinuity

In Figure 6 column (c) we show crossings of the RD model by a synthetic spacecraft (see details of the model in Appendix A.2.1). Rotational discontinuity has an arch-like hodograph (Figure 6, column (c), third row). Discontinuities with an arch-shaped hodograph have been previously observed in the solar wind (Neugebauer 1989; Riley et al. 1996; Tsurutani et al. 1996; Sonnerup et al. 2010; Haaland et al. 2012; Paschmann et al. 2013). In the bottom panel, both ratios  $\lambda_2/\lambda_1 \simeq \lambda_3/\lambda_2 \simeq 0$  when the noise level is low (see dots). For higher noise,  $\lambda_3/\lambda_2$  increases more than  $\lambda_2/\lambda_1$  (see crosses). If the noise level is small enough, so that the MVA eigenvectors ( $\mathbf{e}_1, \mathbf{e}_2, \mathbf{e}_3$ ) are well defined, they coincide with the basis vectors ( $\mathbf{y}, \mathbf{z}, \mathbf{x}$ ) of the reference frame of the sheet (for any crossing trajectory). The magnetic field magnitude is constant across the rotational discontinuity, so it is an incompressible structure.

### 5.2.2. Tangential Discontinuity

Figure 6 column (d) shows the crossing of the tangential discontinuity. The details of the model are described in Appendix A.2.2. Independent of the crossing trajectory the polarization is linear,  $\lambda_2/\lambda_1 \sim 0$ ,  $\lambda_3/\lambda_2 \sim 1$ . Only the maximum MVA eigenvector  $\mathbf{e}_1$  is unambiguously defined; it is tangential to the discontinuity plane ( $\mathbf{e}_1 = \mathbf{y}$ ). The intermediate ( $\mathbf{e}_2$ ) and minimum ( $\mathbf{e}_3$ ) eigenvectors are in the  $x$ - $z$  plane, where  $\mathbf{x}$  and  $\mathbf{z}$  are normal and guide-field directions correspondingly. In this tangential discontinuity model  $B_x = 0$  and  $B_z = \text{const}$ , so  $\delta B_x = \delta B_z = 0$ . Consequently, MVA analysis cannot distinguish between the normal ( $\mathbf{x}$ ) and the guide-field ( $\mathbf{z}$ ) directions. In general, the tangential discontinuity can be asymmetric, separating plasmas with different  $|\mathbf{B}|$ . Thus, the tangential discontinuity can be a compressible structure. Here, we use the simple model, where the value of the magnetic field modulus  $|\mathbf{B}|$  is the same on both sides of the discontinuity.

## 5.3. Magnetic Holes

Magnetic holes are compressible coherent structures, characterized by a localized decrease of the magnetic field modulus. Figure 6, column (e) shows the crossing of the magnetic hole model. The details of the model and some observational properties of magnetic holes are discussed in the Appendix A.3. For any crossing trajectory, the polarization is linear,  $\lambda_2/\lambda_1 \sim 0$ ,  $\lambda_3/\lambda_2 \sim 1$ .

## 6. Examples of the Observed Structures

We consider coherent structures detected by the integrated LIM over all scales and above the threshold,  $I > I_{\text{threshold}}$  (see Section 4.1). Among nearly  $\sim 10^4$  events, we have selected 374 with  $I/I_{\text{threshold}} \geq 6$  for visual examination. All of them have a localized event at sub-ion scales, which is embedded in a larger event at ion scales. In its turn, this ion scale event is embedded in an MHD scale event. This successive embedding, which is

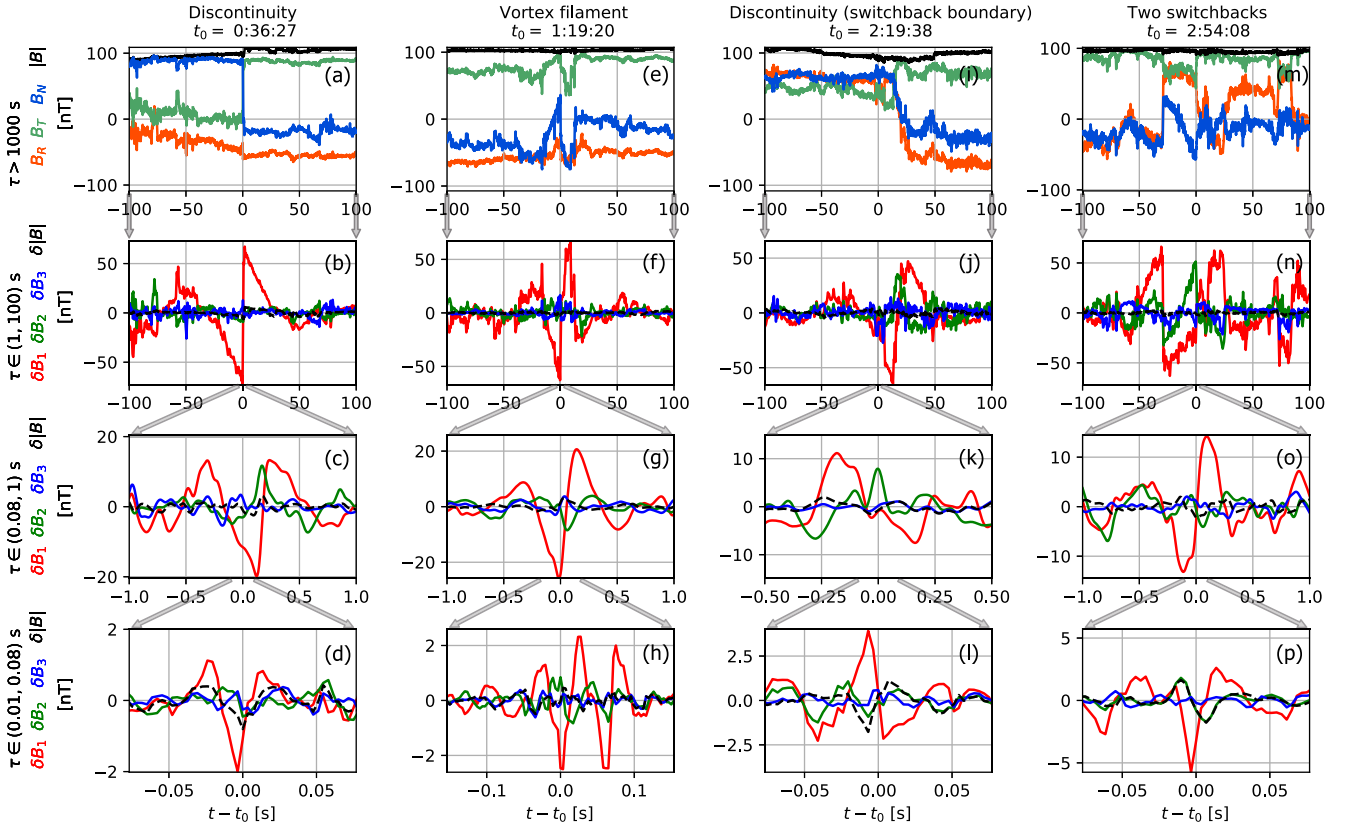


**Figure 7.** Four examples of events detected on 2018 November 6 with integrated  $LIM\ I/I_{\text{threshold}} > 6$  are shown in columns. The central time of each structure  $t_0$  is indicated in the title. Top row: raw magnetic field in the RTN reference frame. Rows 2 through 4: the bandpass-filtered magnetic fluctuations at MHD, ion, and sub-ion frequency ranges in local MVA reference frames. At MHD scales these structures represent: a tangential discontinuity (example 1), an Alfvén vortex (example 2), a rotational discontinuity at the switchback boundary (example 3), and two neighboring switchbacks (example 4). In Appendix B additional information (magnetic fluctuation polarization, Alfvénicity, and plasma parameters) is provided for each event. This information complements the interpretation of the coherent structures. At ion and sub-ion scales magnetic fluctuations can be interpreted as vortex-like structures for the four examples.

shown here for the first time, is like the organization of *Russian dolls*.

In Figure 7 we show four such examples of different types of structures at different scales, found among the subset of 374 events. Here we restrict ourselves to show the magnetic fluctuations only, but the complementary information for each event is presented in Appendix B. It shows the variation of the plasma parameters ( $N_e$ ,  $T_e$ ,  $T_p$ ,  $|V|$ ) across the structure and the Alfvénicity.

We first consider the event in the left column of Figures 7(a)–(d). Panel (a) shows the low-pass-filtered magnetic field in the RTN reference frame during  $\pm 100$  s around the central time with  $t_0 = [00:36:27]$  UT (on 2018 November 6). Using the mean observed velocity  $\sim 340\text{ km s}^{-1}$ , a timescale of 200 s corresponds to a space scale of  $\sim 7 \times 10^4$  km. In this case, the coherent structure around  $(t - t_0) = 0$  is associated with a discontinuity but it is not associated with a switchback boundary, since  $B_R$  is not reversing.

In Figures 7(b)–(d) we show the filtered magnetic field data  $\delta B_j$  at timescales defined by Equation (7), with  $j = \text{“MHD,” “ion,” and “subion.”}$  We use the local MVA reference frame (Sonnerup & Scheible 1998) adapted to each scale range shown. The basis vectors ( $e_1$ ,  $e_2$ ,  $e_3$ ) are directed along the maximum, intermediate, and minimum variance of the magnetic field.

In Figure 7(b), a high-amplitude current sheet is observed at MHD scales. In Appendix B.1 we use the plasma data to provide

a physical analysis as summarized below. In Figures 11(i)–(k) we show that the Walén relation  $\Delta V = \pm \Delta B / \sqrt{4\pi\rho}$  for rotational discontinuities is violated in this example, and the pressure anisotropy correction (Hudson 1970) is insufficient to explain the observation. In addition, the magnetic field magnitude is changing across the sheet; see the black curve in Figure 11(l). The normalized amplitude of the jump is  $\Delta B/B_0 = 0.1$ , where  $\Delta B = |B(t_0 + \Delta t')| - |B(t_0 - \Delta t')| = 10\text{ nT}$ , with  $\Delta t' = 3\text{ s}$ , and  $B_0 = \langle |B| \rangle_{t-t_0 \in (-100, 100)\text{ s}} = 100\text{ nT}$ . This localized jump is  $\approx 2$  times greater than the standard deviation of  $\Delta B/B_0$  in the 5 hr interval. This is also incompatible with the rotational discontinuity, across which the magnetic field magnitude is constant. By contrast, a change in the magnitude of the magnetic field is possible when crossing a tangential discontinuity. So we interpret this structure as a tangential discontinuity. The thickness of this current sheet can be estimated as  $d = V\Delta t = 480\text{ km}$ , or  $100\rho_i$  and  $40d_i$ , where  $\Delta t = 1.5\text{ s}$  is the duration of the current sheet crossing, local  $V = 340\text{ km s}^{-1}$ .

Figures 7(c) and (d) show substructures at ion and sub-ion scales embedded in this tangential discontinuity. Ion scale structure, observed during  $\Delta t = 1\text{ s}$ , resembles crossing the dipole Alfvén vortex model through its center; see Section 5.1.1. The cross-section scale is about  $d = 340\text{ km}$ , or  $60\rho_i$  and  $27d_i$ . The structure, shown in the panel (d) is observed during  $\Delta t = 0.08\text{ s}$ , so the cross-section scale is  $d = 27\text{ km} = 2d_i = 5\rho_i$ . This structure might represent a compressible ion scale Alfvén vortex (Jovanović et al. 2020).

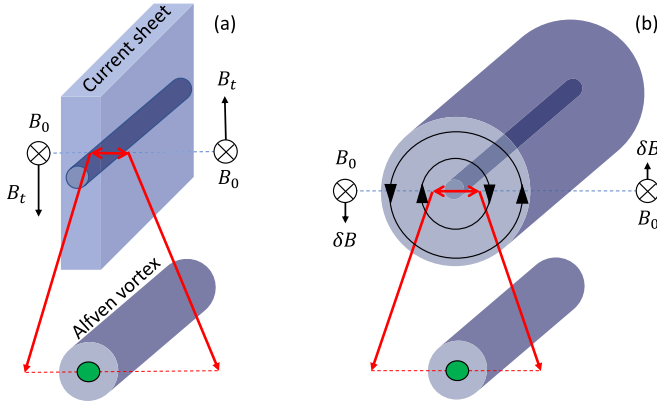


**Figure 8.** Panel (a): Schematic sketch of the Example 1, shown in the Figures 7(a)–(d). The blue dashed line illustrates the crossing trajectory. The mean magnetic field ( $B_0$ ) and the tangential ( $B_t$ ) component are shown in black on both sides of the current sheet. The red lines indicate the zoom to the embedded ion scale vortex. A compressible sub-ion scale vortex is shown in green. The embedded substructures are shown not to scale. Panel (b): sketch of the Example 2, shown in the Figures 7(e)–(h). The magnetic field fluctuations associated with a vortex are shown in black. The embedding of ion and sub-ion scale vortices is shown in the same format as in panel (a).

In this model, vortices have nonzero parallel magnetic fluctuations  $\delta B_{\parallel} \neq 0$  maintained in pressure balance, and the  $\delta B_{\perp}$  fluctuations are similar to the MHD Alfvén vortex. The sketch illustrating the embedding is presented in Figure 8(a).

In Figures 7(e)–(h) the second event around  $t_0 = [01: 19: 20]$  UT is shown in the same format as the first event. Radial magnetic field component  $B_R$  is negative in the center of the structure and during the time interval  $\pm 100$  s (MHD scales). So the MHD scale coherent structure, shown in Figure 7(f), is not associated with a switchback. Its time profile is consistent with the monopole Alfvén vortex crossing close to its center; see the black trajectory in Figure 6(a). The velocity and magnetic field fluctuations are correlated with a proportionality coefficient  $\xi$ ,  $\delta B/B_0 = \xi \delta V/V_A$ , where  $\xi = 0.86 < 1$ ; see Appendix B.2, Figures 12(i)–(k). In the model of the Alfvén vortex,  $\xi$  is a free parameter, simply related to other parameters of the vortex:  $\xi = u/\alpha$ , where  $\alpha$  is the inclination angle of the vortex axis with respect to the background magnetic field, and  $u = V_{\text{vortex}}/V_{\text{th},\perp}$  is the normalized vortex propagation speed in the vortex plane.

The direction of the Alfvén vortex axis can be estimated using MVA if the vortex is crossed by the satellite off-center. In this case, the vortex axis is directed along the direction of the minimum MVA direction  $e_3$ . In the considered example the Alfvén vortex is crossed near the center, and the direction of  $e_3$  (as well as  $e_2$ ) is not reliably determined. However, if we assume that  $e_3$  approximates well the direction of the vortex axis, the inclination angle is  $\alpha = 4^\circ$ . Then, one can estimate the vortex propagation velocity  $u = \xi \cdot \alpha = 0.86 \cdot (4/180 \cdot \pi) = 0.06$ . Thus, with a local proton thermal speed of  $v_{\text{th},\perp} \simeq 50 \text{ km s}^{-1}$ , the vortex propagation velocity is  $V_{\text{vortex}} = 3 \text{ km s}^{-1}$ . This is negligible in comparison with the local bulk solar wind speed  $V = 330 \text{ km s}^{-1}$ , so the vortex is mainly convected across the satellite. Thus, we can use the Taylor hypothesis to estimate its cross-section scale:  $d = V \Delta t \sin \Theta_{BV} = 2.4 \times 10^4 \text{ km}$ , or

$5 \times 10^3 \rho_i$  and  $2 \times 10^3 d_i$ , where  $\Delta t = 80 \text{ s}$  is the duration of the structure and  $\Theta_{BV} = 70^\circ$  is the local field-to-flow angle.

Within this large-scale monopole Alfvén vortex, we observe smaller embedded vortices; see Figures 7(g) and (h). The schematic sketch illustrating this embedding is presented in Figure 8(b). Note that the sketch is not to scale; the diameters of the embedded vortices differ by a factor of 10:  $d = 440 \text{ km} = 90 \rho_i = 40 d_i$  at scales that we call ion scales, and  $d = 47 \text{ km} = 9 \rho_i = 4 d_i$  at so-called sub-ion scales.

Figures 7(i)–(l) shows a third event around  $t_0 = [02: 19: 38]$  UT. In the panel (i),  $B_R$  changes sign across the sheet, meaning that the sheet forms the boundary of a switchback (see the complementary data in Figure 13 and Appendix B.3), similarly to observations by Krasnoselskikh et al. (2020). The current sheet is located at  $t - t_0 = 20 \text{ s}$ ; see Figure 7(j). The velocity and magnetic field jumps satisfy the Walen relation, and the magnetic field magnitude is constant within the short interval  $t - t_0 \in (0, 40) \text{ s}$  near the center of the sheet. So, we conclude that this discontinuity is rotational. The thickness of the current sheet ( $\sim 40 \text{ s}$ ), in terms of spatial scales, corresponds to  $1.4 \times 10^4 \text{ km} = 2 \times 10^3 \rho_i = 1.2 \times 10^3 d_i$ .

Ion scale magnetic fluctuations are shown in Figure 7(k). The minimum variance direction  $e_3$  is along the local mean magnetic field  $B_0 = \langle B \rangle_{t-t_0 \in (-0.5, 0.5) \text{ s}}$ . The maximum ( $\delta B_1$ ) and intermediate ( $\delta B_2$ ) MVA components are perpendicular to  $B_0$  and have similar amplitudes. At the center of the structure ( $t - t_0 = 0$ ),  $\delta B_1$  changes sign, and  $\delta B_2$  has a peak. So, magnetic field fluctuations are in accordance with the off-center crossing of the monopole Alfvén vortex; see the blue trajectory in Figure 6(a). The cross-section scale of the vortex is  $150 \text{ km}$ , or  $\sim 25 \rho_i$  and  $12 d_i$ .

Sub-ion scale structure, Figure 7(l), has typical properties for structures at sub-ion scales in our statistics:  $\delta B_1$  has a Mexican hat-like shape, and this event has a significant compressibility  $\delta|B| \sim 0.5 \delta B_1$ . It is very similar to the sub-ion scale structure shown in Figure 7(d). The cross-section scale of this structure is  $24 \text{ km}$ , or  $4 \rho_i$  and  $2 d_i$ . Such localized compressible magnetic fluctuations at ion scales can be interpreted as the ion Alfvén vortex of Jovanović et al. (2020).

Figures 7(m)–(p) show the fourth example around  $t_0 = [02: 54: 08]$  UT. Our detection method catches two neighboring switchbacks, lasting  $200 \text{ s}$  at MHD scales. Indeed, we see in panel (m) that  $B_R > 0$  during two time intervals in the center, and the rest of the time  $B_R < 0$ . Figure 7(n) shows four current sheets at the boundaries of these switchbacks. The central times of the four current sheets are  $t - t_0 = \{-29, 0, 25, 85\} \text{ s}$ . The complementary information is presented in Appendix B.4.

At ion scales, Figure 7(o), we observe an embedded coherent structure that might represent a monopole Alfvén vortex crossed through the center. The cross-section scale is  $d = 160 \text{ km} = 23 \rho_i = 13 d_i$ . We observe a strong peak-like fluctuation of  $\delta B_1$  at sub-ion scales (see panel (p)). The intermediate MVA fluctuation  $\delta B_2$  is localized in the center of the event. The profile of  $\delta B_2$  is closely similar to the one of  $\delta|B|$ . So, this structure is compressible  $\delta|B| \sim 0.2 \delta B_1$ . The cross-section scale is  $d = 12 \text{ km} \simeq 1.7 \rho_i = d_i$ . It belongs to the same typical class of sub-ion scale coherent structures (compressible ion scale Alfvén vortices) as in other examples.

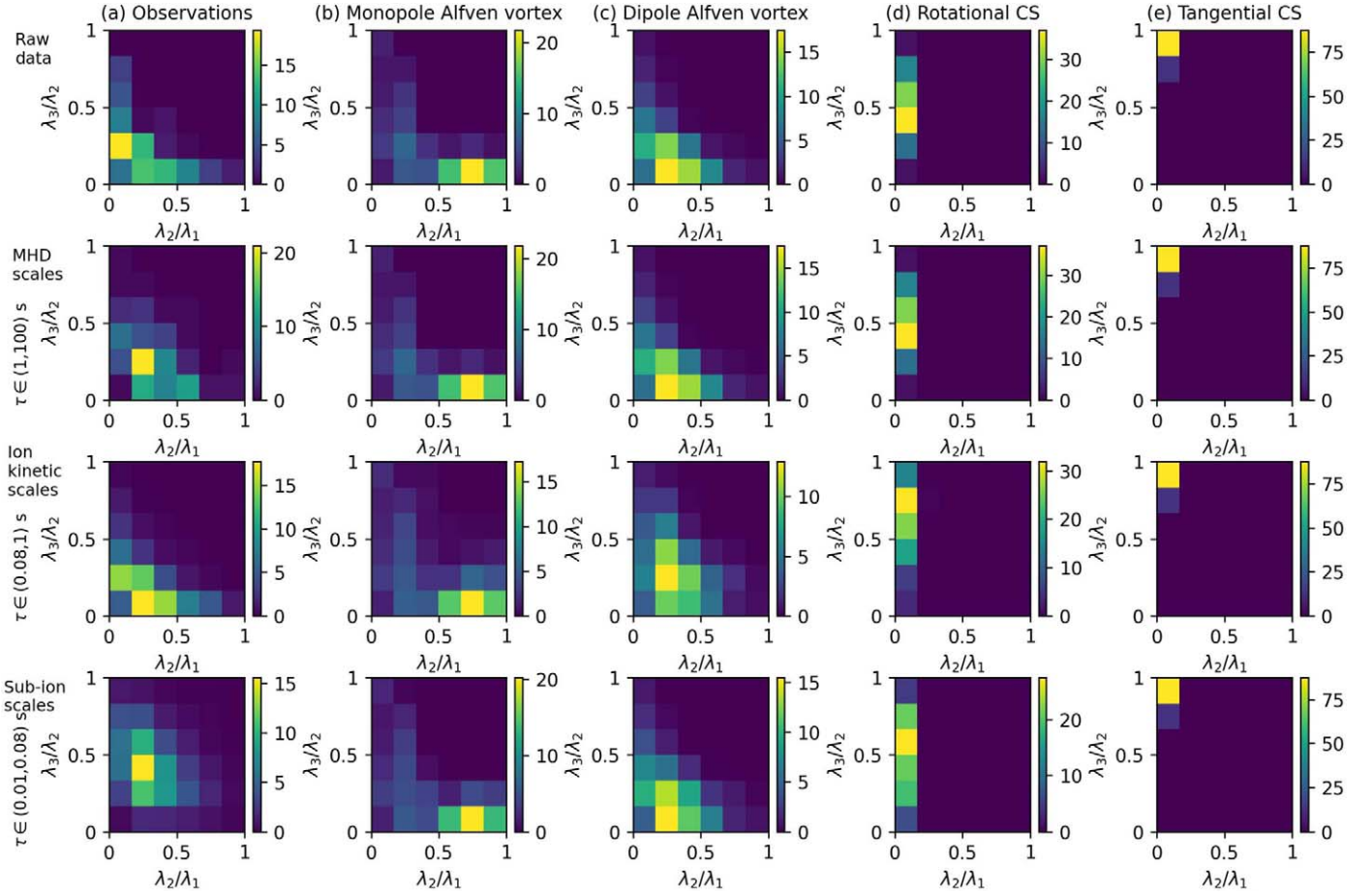


**Figure 9.** Probability distributions on the MVA eigenvalue ratios plane  $(r_{21}, r_{32}) = (\lambda_2/\lambda_1, \lambda_3/\lambda_2)$ . The column (a) shows the probability [%] per bin to observe a coherent structure with the corresponding MVA eigenvalue ratios (so,  $P_{\text{obs}}(r_{21}, r_{32})$ , defined by Equation (17)). The first and second panels of column (a) show the distributions for the MHD scale coherent structures using the raw (nonfiltered) data and the MHD range filtered data, respectively. The third and fourth rows of column (a) correspond to coherent structures detected at ion and sub-ion scale ranges. Columns (b)–(e) show the probability densities obtained from simulating model crossings ( $P(r_{32}, r_{21}|\text{model})$  defined by Equation (18)). The differences between panels of different rows (b)–(e) is due to the different imposed noise levels  $\epsilon_{\text{sim}}$  (see Section 7.2 for details).

## 7. Multiscale Minimum Variance Analysis

Now, we consider the whole set of structures detected by integrated LIM at different timescale ranges; see Equation (11). As we have discussed in Section 4.1, the number of structures increases toward small scales, from nearly 200 events at MHD scales to more than  $10^4$  events at sub-ion scales. For all these events, we study the amplitude anisotropy of the measured fluctuations via MVA (Sonnerup & Scheible 1998). Then, we compare the observed anisotropy with one of the model structures crossed by a spacecraft.

### 7.1. Observational Characteristics of Coherent Structures

For each coherent structure detected at the  $j$ th range of scales we consider filtered magnetic field fluctuations  $\delta\mathbf{B}_j$  at the time interval  $t - t_0 \in T_{\text{struct}} = (-\tau_{\text{max},j}, \tau_{\text{max},j})$  in the vicinity of the structure center  $t_0$ , where  $\tau_{\text{max},j}$  is the maximum timescale of each scale range defined by Equation (7). We define the amplitude of the structure  $\delta\mathbf{B}_{\text{struct},j}$  as:

$$\delta\mathbf{B}_{\text{struct},j} = \max(|\delta\mathbf{B}_j|)_{t \in T_{\text{struct}}}. \quad (14)$$

The amplitude anisotropy of the magnetic fluctuations  $\delta\mathbf{B}_j$  of the structure along the crossing trajectory is characterized by MVA eigenvalue ratios  $\lambda_2/\lambda_1$  and  $\lambda_3/\lambda_2$ . The relative amplitude  $\delta\mathbf{B}_{\text{struct},j}/B_0$  is shown in color in Figure 10. For

each range of scales, the number of structures  $N$  and the filling factor  $P$  (defined in the same way as in Equation (10) but for each scale range) are shown in the legend.

Figure 10(a) gives the results of the MVA for the raw magnetic field data during 200 s time intervals around the central times  $t_0$  of the MHD scale coherent structures (see the discussion of the detection method at the end of Section 4.1). The MVA results for four examples analyzed in detail in Section 6 are marked on the  $(\lambda_2/\lambda_1, \lambda_3/\lambda_2)$  plane with special symbols: example 1, TD at large scales, is a black dot; example 2, an Alfvén vortex at large scales, is a cross; example 3, an RD at large scales, is a plus; example 4, two neighboring switchbacks, is a circled dot.

For a large number of events, the ratio of the minimum over intermediate eigenvalues is small,  $\lambda_3/\lambda_2 < 0.5$ , while intermediate over maximum variance,  $\lambda_2/\lambda_1$ , takes the whole range of values from 0 to 1. Among the considered models, this zone on the eigenvalue plane corresponds only to the monopole and dipole Alfvén vortices; see Figure 6. Minimum over intermediate variance,  $\lambda_3/\lambda_2$ , sometimes takes high values ( $> 0.5$ ), as is the case for the monopole vortex, a tangential discontinuity, or a magnetic hole. Values of  $\lambda_3/\lambda_2$  around 0.3 and for small  $\lambda_2/\lambda_1$  can be interpreted as rotational discontinuities; see Figure 6. So, the observed distribution of  $\lambda_3/\lambda_2$  as a function of  $\lambda_2/\lambda_1$  can be due to a superposition of

**Table 2**

The Mean and the Standard Deviation of the Relative Noise Level  $\epsilon_{\text{obs}}$  at Different Ranges of Scales

Range of Scales	$\langle \epsilon_{\text{obs}} \rangle$	$\sigma(\epsilon_{\text{obs},j})$
RAWDATA MHD	0.11	0.03
MHD	0.11	0.03
Ion scales	0.15	0.05
Sub-ion	0.12	0.03

different types of coherent structures. It seems that vortices are dominant, but other types of structures may also exist.

Figure 10(b) corresponds to the same set of coherent structures as in panel (a) but for filtered MHD scale fluctuations  $\delta \mathbf{B}_{\text{MHD}}$  instead of the raw magnetic field data. Here, the data are spread nearly uniformly in the bottom-left part of the panel. This distribution can be also interpreted as a superposition of the five models discussed above, with a dominance of vortices.

Figures 10(c) and (d) represent the MVA results for ion and sub-ion scale structures, respectively. At ion scales, the distribution is similar to what is observed in raw data, but with more cases (2028 versus 196). Sub-ion scale structures have different distributions on the MVA eigenvalue ratios. Most of the points (especially yellow ones, corresponding to high-amplitude events) are grouped closer to the left part of the eigenvalue plane, where  $\lambda_2/\lambda_1 < 0.25$ . But this does not exclude any of the five models.

Below, in Sections 7.2 and 7.3, we propose a new systematic approach to quantify the proportions of different types of structures at different scales.

### 7.2. Noise Level Estimation

We want to compare the observed distributions of  $(\lambda_2/\lambda_1, \lambda_3/\lambda_2)$  and the degree of compressibility (defined below in Equation (15)) for MHD, ion, and sub-ion scale structures, with the crossings of different coherent structures models (see Section 5). The incoherent noise affects the MVA eigenvalue ratios (shown in the bottom row of Figure 6). The greater the ratio  $\epsilon = \delta \mathbf{B}_{\text{noise}}/\delta \mathbf{B}_{\text{struct}}$ , the closer are the  $\lambda_2/\lambda_1$  and  $\lambda_3/\lambda_2$  to 1. Therefore, we need to estimate  $\epsilon$  from observations to take into account the noise in the model crossings.

For each structure at the  $j$ th scale range, we calculate the ratio of the noise  $\sigma_{\text{noise},j}$ , defined in Equation (12), to the amplitude of the structure  $\delta \mathbf{B}_{\text{struct},j}$ :

$$\epsilon_{\text{obs},j} = \sigma_{\text{noise},j}/\delta \mathbf{B}_{\text{struct},j}. \quad (15)$$

At each range of scales the distribution of  $\epsilon_{\text{obs},j}$  is nearly Gaussian, but with different values of parameters. The mean values  $\langle \epsilon_{\text{obs},j} \rangle$  and the standard deviations  $\sigma(\epsilon_{\text{obs},j})$  are shown in Table 2.

We repeated the crossings simulation with 10 different relative amplitudes of the imposed noise  $\epsilon_{\text{sim}}$  following the Gaussian distribution with the same parameters,  $\langle \epsilon_{\text{obs},j} \rangle$  and  $\sigma(\epsilon_{\text{obs},j})$ , as in observations. The obtained results of the model crossings with different  $\epsilon_{\text{sim}}$  are used in the next section.

### 7.3. Classification

For convenience we use the notation  $(r_{21}, r_{32}) = (\lambda_2/\lambda_1, \lambda_3/\lambda_2)$  for MVA eigenvalue ratios. First, we investigate the presence of magnetic holes. We use two criteria to select magnetic holes: high compressibility and linear polarization.

A coherent structure is compressible if the magnetic field modulus  $|\mathbf{B}|$  is not constant because of the parallel magnetic fluctuations of the structure. Considering the compressibility at the  $j$ th range of scales, we filter  $|\mathbf{B}|$  (as we do for fluctuations  $\delta \mathbf{B}_j$ ) to define  $\delta |\mathbf{B}|$  at the scale range  $j$ . The amplitude of compression associated with a coherent structure is given as  $\max(|\delta |\mathbf{B}||)_{r \in \mathcal{T}_{\text{struct}}}$ . We normalize it by  $\delta \mathbf{B}_{\text{struct}}$  to define the compressibility of the structure:

$$C_{\text{struct}} = \max(|\delta |\mathbf{B}||)/\delta \mathbf{B}_{\text{struct}}. \quad (16)$$

We underline that our definition of compressibility differs from the definitions used in Turner et al. (1977) and Volwerk et al. (2020). It is more similar to those used in Stevens & Kasper (2007) and Perrone et al. (2016).

First, we impose  $C_{\text{struct}} > 0.8$  to select strongly compressible structures and, second, we delimit the zone ( $r_{32} > 0.6$ ,  $r_{21} < 0.4$ ) in the MVA eigenvalue ratios plane, which is characteristic for the magnetic hole crossings; see the bottom panel of the Figure 6(e). This zone is a bit wider than in Figure 6(e), because for some of the magnetic holes in the observational statistics the relative noise amplitude could be higher than  $\epsilon = 0.1$ , as used in the model. The percentage of MHD, ion, and sub-ion structures satisfying both criteria is presented in the column ‘‘Magnetic Hole’’ of Table 3. We found that magnetic holes are detected only at sub-ion scales. Among sub-ion scale structures, they account for 0.4% of the cases. We will study these events in more detail in future work.

We define the proportions of vortices and current sheets among the remaining observed structures by comparing the amplitude anisotropy from observation, without imposing any criterion for compressibility.

Figure 9(a) shows 2D histograms ( $6 \times 6$  bins) of distributions of the data in the  $(r_{21}, r_{32})$  plane for observations at MHD (top), ion (middle), and sub-ion (bottom) scales. In other words, we show the probability density  $P_{\text{obs},j}$  of observations

$$P_{\text{obs},j}(r_{21}, r_{32}) = N_{\text{obs},j}(r_{21}, r_{32})/N_{\text{obs},j}, \quad (17)$$

where  $N_{\text{obs},j}(r_{21}, r_{32})$  is the number of the observed structures in a bin, and  $N_{\text{obs},j}$  is the total number of observed structures. The index  $j$  denotes the scale range.

We assume that crossings of coherent structures along trajectories with different impact parameters are equally probable, and we take into account the noise from the observations, with Equation (15), as explained below. Since the dipole Alfvén vortex has an angular structure, we average the results over a uniform distribution of trajectory orientations. Then, we obtain the probability density  $P(r_{21}, r_{32} | \text{mod})$  of the MVA eigenvalue ratios for each model structure:

$$P_j(r_{21}, r_{32} | \text{mod}) = N_{\text{mod},j}(r_{21}, r_{32})/N_{\text{mod},j}. \quad (18)$$

The probability distributions for four different models  $P_j(r_{21}, r_{32} | \text{mod})$  are shown in columns (b)–(e) of Figure 9. To simulate different scales, we change the noise level according to the estimated value at each scale; see Equation (15).

The observed distribution of MVA eigenvalue ratios  $P_{\text{obs},j}$  can be expressed as the linear combination of the conditional probabilities  $P_j(r_{21}, r_{32} | \text{mod})$ , determined from the models. The positive coefficients  $p_{\text{mod}}$  reflect the probability to encounter each model structure. Coefficients  $p_{\text{mod}}$  are found

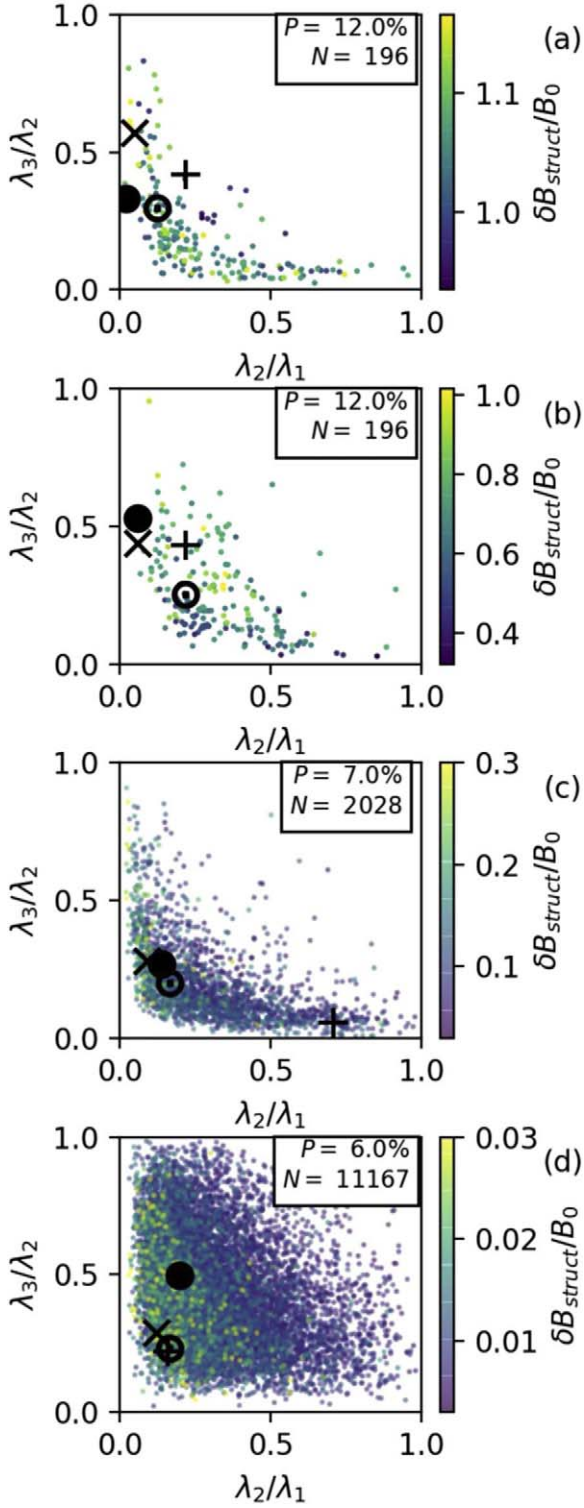


**Figure 10.** Minimum variance analysis eigenvalues ratios plane ( $\lambda_2/\lambda_1$ ,  $\lambda_3/\lambda_2$ ): each dot corresponds to an observed coherent structure, and the color gives its amplitude  $\delta B_{\text{struct}}/B_0$  (see Equation (14)). Panels (a) and (b) correspond to the raw data and MHD scales, respectively. They include 196 structures found at MHD scales. Panel (c) gives the results for 2028 structures at ion scales, and panel (d) gives the eigenvalues ratios for 11,167 events at sub-ion scales. The filling factor  $P$  and the number of detected coherent structures  $N$  at different frequency ranges are shown in the legends. The eigenvalue ratios of the example structures 1–4 from Figure 7 are shown by the black marks: “circle,” “cross,” “plus,” and “odot.”

from the constrained minimization problem:

$$\begin{cases} \|\|P_{\text{obs}}(r_{21}, r_{32}) - \sum_{\text{mod}} p_{\text{mod}} P(r_{21}, r_{32} | \text{mod})\|\| \rightarrow 0 \\ \sum_{\text{mod}} p_{\text{mod}} \leq 1 \\ p_{\text{mod}} \geq 0 \end{cases} \quad (19)$$

where  $\|\cdot\|$  means a norm (the square root of the square of the difference of the matrix) that allow us to use the least squares minimization. The problem is solved for each range of scales. For convenience, the index  $j$  is omitted in Equation (19).

The resulting probabilities  $p_{\text{mod}}$  are shown in the Table 3. For each range of scales, the observations are most consistent with the crossings of the dipole Alfvén vortices ( $\geq 80\%$ ). The monopole vortices account for a small fraction of coherent structures, 7%–15% depending on the scale range. The rotational discontinuities are observed in raw (nonfiltered) data at MHD scales only, but not in the MHD bandpass-filtered data. This is because the bandpass filter makes the waveforms very different from the current sheet simple model; see Figure 7(b). Tangential discontinuities do not appear to be statistically significant. In all, 6% of events were not possible to model at MHD scales, and 39% at sub-ion scales (see the *None* column in Table 3). This unidentified large number of events at sub-ion scales is probably due to a more three-dimensional nature of the fluctuations not taken into account by nearly incompressible models with mostly  $\delta B_{\perp}$  fluctuations.

The result presented in Table 3 does not change qualitatively if, instead of least squares, the sum of the absolute values of probability differences (between observations and models) in each bin is minimized.

Let us compare the obtained results with the previous observations. The visual classification of ion scale coherent structures at 0.17 au, during the first PSP perihelion, has been done recently in Perrone et al. (2020). Three different time intervals were considered: quiet, weakly disturbed, and highly disturbed solar wind. The highly disturbed interval (of 1.5 hr) with  $B_R$  reversals is a subset of the 5 hr interval considered here. The authors concluded that in the highly disturbed interval current sheets were dominant (46%), while during the weakly disturbed interval Alfvén vortices (45%) and wave packets (50%) were observed. This is in contrast to the quantitative classification results obtained here at ion scales, showing that Alfvén vortices are dominant.

In the previous studies of ion scale coherent structures at 1 au in the slow (Perrone et al. 2016) and fast (Perrone et al. 2017) solar wind with Cluster satellites, the dominance of Alfvén vortices with respect to current sheets has been found. This is more consistent with our results at 0.17 au in the slow wind.

We have visually analyzed 196 MHD scale coherent structures to understand why the percentage of current sheets is low. We remind the reader that the peaks of the integrated LIM over the MHD range (between 1 and 100 s) determine the central times of the structures. The time interval for each structure is  $\pm 100$  s around the central time, and the corresponding spatial scale is  $\sim 7 \times 10^4$  km. The results are summarized in the Table 4. We realized that the observed events need to be separated in isolated and non-isolated structures, such as a train of Alfvén vortices (see the second column “Multiple Alfvén vortices”) or non-isolated

**Table 3**  
Relative Proportions of Different Structures Seen at Different Scales

Range of Scales	$N$	$P$ (%)	Alfvén Vortex		Current Sheet		Magnetic Hole	None
			Monopole	Dipole	Rotational	Tangential		
Raw data MHD	196	12	0.04	0.86	0.1	0	0	0
MHD	196	12	0.1	0.84	0.0	0	0	0.06
Ion scales	2028	7	0.15	0.85	0.0	0	0	0
Sub-ion	11,167	6	0.07	0.49	0.05	0	0.004	0.39

**Note.** In the first and second columns, we give the number of structures  $N$  and the filling factor  $P$  (%) at different ranges of scales (as defined in Section 4.1). Other columns give results of the problem formulated in Equation (19): the coefficients  $p_{\text{mod}}$  correspond to the fraction of the observed coherent structures that have MVA eigenvalue ratios and compressibility consistent with the crossing of a given model (Figure 6).

**Table 4**  
Fraction of the MHD Structures Obtained by Visual Classification of 196 Events at These Scales

Range of Scales	Alfvén Vortex		Vortex+Current Sheet	Current Sheet		Unidentified
	Isolated	Multiple		Isolated	Non-isolated	
Raw data and MHD	0.24 (0.03)	0.16 (0.03)	0.26 (0.08)	0.03 (0.005)	0.10 (0.05)	0.21

**Note.** We give the fraction of the switchbacks in the parentheses. In total, 19% of events at MHD scales are parts of switchbacks.

current sheets (column 5), and as well we observe a coexistence of a large-scale weak current sheet with a vortex inside (column 3). So, in comparison with an automatic classification (Table 3), here we observe more current sheets; most of them are associated with a vortex (51 cases out of 196), but, as well, six isolated current sheets that have been detected in raw data but not at MHD scales. For the non-isolated current sheets and especially those associated with a vortex, the automatic classification tends to interpret the structures as Alfvén vortices.

Indeed, if the current sheet is not isolated, the perturbations of the neighboring structure affect the MVA eigenvalue ratios, so that the structure is shifted away from the characteristic zone on the  $(r_{21}, r_{32})$  plane; see Figure 6. Consequently, these events contribute to  $p_{\text{monopole}}$  and  $p_{\text{dipole}}$  in the solution of the minimization problem (Equation (19)).

Finally, for the 196 events, we have visually inspected ion and sub-ion scale substructures. Their shape is consistent with vortex crossings and not with current sheets. This is in agreement with Table 3.

## 8. Conclusion and Discussions

The intermittency in the solar wind is typically investigated from the statistical point of view. The scale-dependent kurtosis of magnetic increments is used as the principal quantitative diagnostic, showing the presence of coherent structures.

In this paper, for the first time, we apply a multiscale approach in physical space, from the largest MHD scales  $\sim 10^5$  km to the smallest resolved sub-ion scales  $\sim 3$  km.

Using PSP merged magnetic field data at 0.17 au and the Morlet wavelet transform, we detect intermittent coherent structures covering all scales. We find localized magnetic fluctuations on sub-ion scales with amplitudes of up to  $\delta B/B_0 \sim 0.03$ , where  $B_0$  is the local magnetic field strength. These small-scale structures are typically embedded in a larger structure at ion scales, with amplitudes of up to  $\delta B/B_0 \sim 0.3$ . At its turn, the ion scale structure is embedded in a high-amplitude ( $\delta B_{\text{struct}}/B_0 \sim 0.4\text{--}1.0$ ) MHD scale structure. Such embedding across the whole turbulent cascade is presented here for the first time.

The topology and properties of the coherent structures change from scale to scale. Using plasma and magnetic field time profiles, we characterize several events in more detail. We show examples of planar tangential and rotational discontinuities at MHD scales with the thickness of about  $100\rho_i$  containing embedded substructures inside them: an incompressible ion scale Alfvén vortex (with a cross section of  $\simeq 30\rho_i$ ) and a sub-ion scale compressible vortex  $\simeq 5\rho_i$ ; see the sketch in Figure 8(a). Another example is an Alfvén vortex at MHD scales with the cross section of  $5 \times 10^3\rho_i$ , with embedded incompressible vortices of  $60\rho_i$  at ion and of  $\sim 10\rho_i$  at sub-ion scales; see the sketch in Figure 8(b).

We completed the study of examples with a statistical analysis. In a time interval of about 5 hr we detected nearly 200 events at the MHD scales, and many more events at ion ( $\sim 2 \times 10^3$ ) and sub-ion scales ( $\sim 10^4$ ). The filling factor of the structures, which we estimate in a conservative way<sup>6</sup> (see discussion in Section 4.1), decreases from 12% at MHD scales to 7% and 6% at ion and sub-ion scales correspondingly.

To determine the dominant type of coherent structures, we perform an automatic classification based on the comparison of the observed amplitude anisotropy of magnetic fluctuations within the observed events at all scales with analytical models of Alfvén vortices, current sheets, and magnetic holes. We do not consider magnetosonic shocks, as the analyzed time interval is mostly incompressible at MHD scales. The results show the dominance of Alfvén vortices at all scales and only a few current sheets, and mostly in raw data.

In order to understand the low number of current sheets, we did a visual inspection of 196 events at MHD scales. It reveals that isolated current sheets are indeed rare (3%). Most of the events are rather complex. About 10% of structures represent non-isolated current sheets. Many of the detected events are vortices within the current sheets (26%). Isolated and non-

<sup>6</sup> Using only the time where the integrated LIM is over the threshold means that the lower-energy part of each event is not taken into account in the calculation of the filling factor. If the method of Perrone et al. (2016) was used, the filling factor would be 2–3 times larger.

isolated vortices account for 66% of the structures. In all these cases, except isolated current sheets, the automatic classification method tends to interpret the data as vortices.

The ion transition range of scales corresponds to [30, 340] km or [5, 70] $\rho_i$  in our time interval. Here, with the automatic classification method, we found 85% dipole vortices and 15% of monopoles. Planar discontinuities are not found by our method. Visual inspection of 196 cases confirms the absence of current sheets at these scales.

On sub-ion scales ([3, 30] km or [0.5, 5] $\rho_i$ ) coherent structures represent dipole vortices (49%), monopole vortices (7%), rotational current sheets (5%), and magnetic holes (0.4%). Around 39% of sub-ion scale structures do not fit any of the considered models. It is, possibly, because the incompressible models of vortices have been used to compare with the observations. To improve this study at these scales in the future, the compressible ion scales Alfvén vortex model of Jovanović et al. (2020) should be used. In this model, together with typical vortical  $\delta\mathbf{B}_\perp$ , the compressible component  $\delta B_\parallel$  appears, which is in pressure balance with density fluctuations. We presume that the comparison with this model will increase the proportion of the vortices at sub-ion scales.

Results presented in this article show the dominance of Alfvén vortices at all scales: from inertial to sub-ion range. Thus, Alfvén vortices are important building blocks of solar wind turbulence and in particular of its intermittency at all scales. Alfvén vortices can explain  $\delta\mathbf{V}_\perp/V_A = \xi \delta\mathbf{B}_\perp/B_0$ , with  $\xi \neq 1$ , typically observed in the solar wind for Alfvénic periods.

In the reflection-driven turbulence in the reduced magneto-hydrodynamic numerical simulation of Meyrand et al. (2023), the authors observe *cellularization* of turbulence with generation of magnetic vortices with  $\delta\mathbf{V}_\perp = 0$ , with  $k_\parallel = 0$  and with magnetic field discontinuity at the vortex boundary. These structures are thus quite different from the smooth Alfvén vortices observed here with  $\delta\mathbf{B}_\perp \sim \delta\mathbf{V}_\perp$  correlations, but they have a similar twisted magnetic field configuration and  $k_\parallel = 0$ .

Our results are limited to a specific slow, highly perturbed solar wind region at 0.17 au from the Sun. The analysis can be expanded to different solar wind conditions (different radial distances, types of solar wind, and origins from ecliptic or polar regions of the Sun) to obtain a more general picture.

The multiscale nature of coherent structures described in this article can be studied in the future by the Helioswarm (NASA mission). It will cover MHD, ion, and sub-ion scales at the same time.

## Acknowledgments

We thank the reviewer for their careful reading and analysis of our paper. The comments were very helpful to improve the paper. A.V. acknowledges funding support from the Initiative Physique des Infinis (IPI), a research training program of the Idex SUPER at Sorbonne Université. O.A. acknowledges funding support from CNES. Wavelet software was provided by C. Torrence and G. Compo and is available at <http://atoc.colorado.edu/research/wavelets/>.

## Appendix A Model Structures

### A.1. Alfvén Vortices

Alfvén vortices, introduced by Petviashvili & Pokhotelov (1992), are cylindrical magnetic structures with Alfvénic

properties, i.e., with correlated (or anticorrelated) transverse magnetic and velocity perturbations, and with current aligned (or antialigned) with vorticity. The model of Alfvén vortices is based on the reduced MHD equations (Kadomtsev & Pogutse 1974; Strauss 1976), where the principal assumptions are the perpendicular anisotropy in the wavevector space,  $k_\perp \gg k_\parallel$ , and slow time variations,  $d/dt \ll f_{ci}$ . Two main types of vortices are distinguished: monopolar and dipolar.

Let the axis  $z$  be along the background magnetic field  $\mathbf{B}_0$ . The transverse magnetic field  $\delta\mathbf{B}_\perp = \nabla A_z \times \mathbf{z}$  and velocity  $\delta\mathbf{V}_\perp = \mathbf{z} \times \nabla\psi$  perturbations are expressed with the axial component of the vector potential  $A_z$  and the velocity flux function  $\psi$ . The model assumes linear proportionality  $\psi = \xi A_z$ , or equivalently  $\delta\mathbf{V}_\perp/V_A = \xi \delta\mathbf{B}_\perp/B_0$  (generalized Alfvén relation).

#### A.1.1. Monopole Alfvén Vortex

A monopole Alfvén vortex is localized within the cylinder of the radius  $a$ , and the axis of the cylinder is aligned with  $\mathbf{B}_0$ . The model assumes that the total current inside  $r < a$  is zero. If  $\delta\mathbf{B}_\perp$  is continuous at  $r = a$ , it implies the condition  $J_1(ka) = 0$ , where  $J_1$  is the first-order Bessel function. This defines the parameter  $k$  for a given radius  $a$ . The monopole vortex solution writes (in dimensionless units; see Petviashvili & Pokhotelov 1992):

$$\begin{cases} A_z = A_0(J_0(kr) - J_0(ka)), & r < a \\ A_z = 0, & r > a \end{cases} \quad (\text{A1})$$

where  $A_0$  is the monopole vortex amplitude and  $J_0$  is the zero-order Bessel function.

A monopole Alfvén vortex in the plane perpendicular to its axis is shown in the top panel of Figure 6(a). The amplitude of the structure,  $\delta B_\perp/B_0 = 0.5$ , is taken to be comparable to the observations (see Figure 12(b)).

#### A.1.2. Dipole Alfvén Vortex

As in the case of the monopole vortex, the dipole vortex is a coherent structure localized inside the cylinder of radius  $a$ , and the generalized Alfvén relation  $\delta\mathbf{V}_\perp/V_A = \xi \delta\mathbf{B}_\perp/B_0$  is assumed.

The particular property of the dipole Alfvén vortex model is that its axis can be inclined by a small angle  $\theta$  with respect to the background magnetic field  $B_z = B_0$ . We define  $\alpha = \tan(\theta)$ . Without restriction of generality, let the axis of the vortex be in the  $(y, z)$  plane. If  $\theta \neq 0$ , the dipole vortex propagates along  $y$  with the speed  $u \propto \alpha$ . The continuity of  $\delta\mathbf{B}_\perp$  at  $r = a$  requires that the amplitude of the dipole vortex is not arbitrary, but defined by  $\alpha$  and  $k$ .

In the reference frame moving with the vortex, the dimensionless vector potential of the dipole vortex is (Petviashvili & Pokhotelov 1992; Alexandrova 2008):

$$\begin{cases} A_z = \frac{-2\alpha}{kJ_0(ka)} J_1(kr) \frac{x}{r} + \alpha x, & r < a \\ A_z = \alpha x \frac{a^2}{r^2}, & r > a. \end{cases} \quad (\text{A2})$$

A dipole Alfvén vortex is shown in Figure 6(b).

### A.2. Current Sheets

Current sheets are planar coherent structures that separate the plasma with different magnetic field directions. Current sheets with large rotation angles across the sheet represent the



boundaries of magnetic tubes, according to Bruno et al. (2001) and Borovsky (2008). The population of current sheets with smaller rotation angles is much more numerous (Borovsky 2008). They might be formed spontaneously as a result of the turbulent cascade (e.g., Veltri 1999; Mangeney 2001; Veltri et al. 2005; Greco et al. 2008, 2009, 2012; Servidio et al. 2008; Salem et al. 2009; Zhdankin et al. 2012).

MHD classification of current sheets includes rotational and tangential discontinuities (RDs and TDs, respectively; e.g., Baumjohann & Treumann 1997; Tsurutani et al. 2011). A typical method to distinguish RDs from TDs is based on the normalized change in magnetic field magnitude  $\Delta B/B$  across the discontinuity (which is zero for RD) and the normal magnetic field component  $B_n/B$  (which is zero for TD). To test the criterion  $B_n/B=0$ , the normal to the sheet must be accurately determined. Current sheets are planar structures, so  $B_n = \text{const}$  (due to the divergence-free magnetic field). Therefore, the direction of the normal ( $\mathbf{n}$ ) can be estimated using MVA, namely  $\mathbf{n} = \mathbf{e}_3$ . However, the error of this method is significant (Horbury et al. 2001; Knetter et al. 2004; Wang et al. 2024). Thus, the verification of the criterion by MVA in application to single-spacecraft data is not accurate enough to classify the current sheets in the solar wind as tangential or rotational. Observations showed that current sheets can combine the properties of RDs and TDs, so classifying them as RDs or TDs might be an oversimplification (e.g., Neugebauer 2006; Artemyev et al. 2019).

#### A.2.1. Rotational Discontinuity

RDs are characterized by the correlated rotation of magnetic field and velocity (Walen relation in the case of the pressure isotropy:  $\delta\mathbf{B}/B_0 = \pm\delta\mathbf{V}/V_A$ ), and constant magnetic and plasma pressures across the sheet ( $\Delta B/B = \Delta P/P = 0$ ). Plasma on both sides of an RD is magnetically connected, i.e.,  $B_n \neq 0$ .

Let the normal to the current sheet  $\mathbf{n}$  be along  $\mathbf{e}_x$ , and  $B_n$  and  $B_t$  denote normal and tangential magnetic field components. The condition  $\nabla \cdot \mathbf{B} = 0$  implies  $B_x = B_n = \text{constant}$ . We use the same rotational discontinuity model as in Goodrich & Cargill (1991), where the magnetic field rotates smoothly by an angle  $\zeta(x/\ell) = \Delta\zeta/2 \tanh(x/\ell)$  with a total angle  $\Delta\zeta$  across the RD with thickness  $\ell$ :

$$\begin{cases} B_x(x) = B_n \\ B_y(x) = B_t \cos(\zeta(x/\ell)) \\ B_z(x) = B_t \sin(\zeta(x/\ell)) \end{cases} \quad (\text{A3})$$

We select  $\Delta\zeta = 120^\circ$  as in the example that we discuss in Appendix B.3. According to the statistical study of the current sheets from the first PSP perihelion, thin current sheets have smaller magnetic field rotation angles  $\Delta\zeta \sim 21^\circ \times (\ell/d_i)^{0.32}$ , where  $\ell$  is the current sheet (CS) thickness and  $d_i$  is the proton inertial length (Lotekar et al. 2022). For rotational discontinuities with smaller  $\Delta\zeta$  the polarization becomes closer to linear, i.e., closer to the case of the tangential discontinuity model discussed in Appendix A.2.2. In terms of eigenvalues,  $\lambda_3/\lambda_2$  increases while  $\Delta\zeta$  decreases. The selection of  $\Delta\zeta = 120^\circ$  corresponds to a high-amplitude RD. The RDs with small  $\Delta\zeta$  cannot be distinguished from TDs with the polarization and MVA eigenvalue ratios.

#### A.2.2. Tangential Discontinuity

TDs separate two magnetically disconnected plasma regions, so the normal component of the magnetic field is zero,  $B_x = B_n = 0$ . We use the Harris-like current sheet model, with a constant guide field  $B_z = B_0$  (Harris 1962):

$$\begin{cases} B_x = 0 \\ B_y = B_t \tanh(x/\ell) \\ B_z = B_0 \end{cases} \quad (\text{A4})$$

In the presence of the strong guide field  $B_0 \gg B_t$ , the current density is quasi-parallel to the magnetic field. So, the current sheet is quasi-force-free in accordance with what was found in observations (Artemyev et al. 2019).

#### A.3. Magnetic Holes

A magnetic hole represents a localized magnetic field modulus decrease. MHD scale magnetic holes (with cross-section widths ranging from  $\sim 10\rho_p$  to  $\sim 10^3\rho_p$ , where  $\rho_p$  is the proton Larmor radius), are quite rare events: at 1 au the occurrence rate of 0.6 per day was observed by Stevens & Kasper (2007). Closer to the Sun the occurrence rate is higher: 2.4 per day at 0.7 au and 3.4 per day at 0.3 au (Volwerk et al. 2020).

MMS solar wind observations (Wang et al. 2020) and kinetic simulations (Haynes et al. 2015; Roytershteyn et al. 2015) have found magnetic holes at sub-ion scales. Particle-in-cell simulations show that magnetic holes (defined as regions of magnetic field depression) tend to have cylindrical field-aligned geometry (Haynes et al. 2015; Roytershteyn et al. 2015).

We consider the magnetic hole model where the magnetic field direction does not change across the structure (linear magnetic hole). We suppose that the hole has cylindrical geometry and the axis is along  $\mathbf{e}_z$ . The radius of the hole is designated as  $a$ .

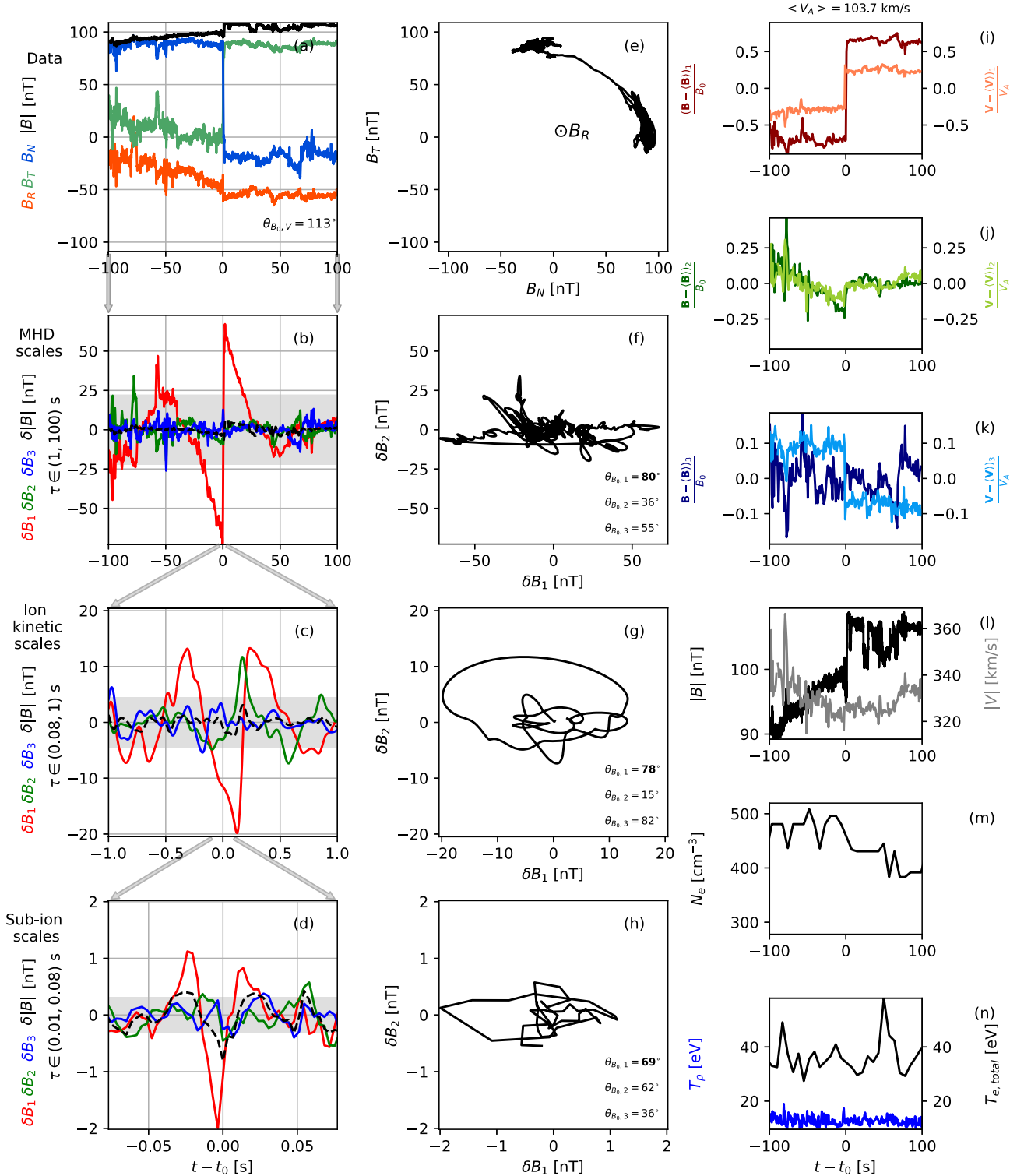
$$\begin{cases} B_x = 0 \\ B_y = 0 \\ B_z = B_0 - \delta B_{\parallel} / \cosh((x/a)^2 + (y/a)^2) \end{cases} \quad (\text{A5})$$

## Appendix B Examples of Structures

### B.1. Example 1

The first event was observed on 2018 November 6 at  $t_0 = 00:36:27$  UT. Figure 11(a) shows magnetic field data in the RTN reference frame during 200 s around  $t_0$ . Here,  $B_T$  and  $B_N$  components change sign in the center, and the magnetic field rotates by the angle  $\Delta\zeta = 80^\circ$ . Thus, this is an example of a current sheet. PSP crosses this current sheet in  $\Delta t \simeq 1.5$  s, so its thickness is about  $V\Delta t \sim 450$  km. The flow-to-field angle is  $\Theta_{BV} = 113^\circ$ , so the PSP crosses this structure under a quasi-perpendicular angle. The polarization of the fluctuations in the plane ( $B_N$ ,  $B_T$ ) is shown in panel (e). The out-of-plane  $B_R$  is negative and nearly constant during the considered time interval, so this discontinuity is not at the edge of a switchback.

Figure 11(b) shows bandpass-filtered MHD inertial range magnetic fluctuations  $\delta\mathbf{B}_{\text{MHD}}$  during the same 200 s around  $t_0$  in the MVA reference frame. The gray horizontal bands indicate  $\pm 2\sigma_{\text{MHD}}$  (two standard deviations of the random-phase signal at MHD scales). The discontinuity in the center is

$t_0 = 0:36:27$ 

**Figure 11.** Example 1: a tangential discontinuity on MHD scales. The four panels on the left represent magnetic fluctuations near the central time  $t_0 = 0:36:27$  UT. (a) Original magnetic field in the RTN reference frame; (b) bandpass-filtered magnetic fluctuations at MHD; (c) ion and (d) sub-ion frequency ranges (see Equations (6) and (7) in local MVA reference frame); (e)–(h) corresponding polarization plots. The orientation of MVA basis vectors  $\{e_i\}_{i=1,2,3}$  with respect to the background magnetic field  $\mathbf{B}_0$  is provided in the legend with  $\theta_{B_0,i}$  angles. Angles for well-defined MVA basis vectors are shown in bold. Panels of the right column show different plasma parameters at MHD scales: (i)–(k) the correlation between  $(\mathbf{B} - \langle \mathbf{B} \rangle) / B_0$  and  $(\mathbf{V} - \langle \mathbf{V} \rangle) / V_A$ ; (l) the magnetic field and velocity modulus ( $|\mathbf{B}|$  and  $|\mathbf{V}|$ ); (m) the electron density  $N_e$ ; (n) proton and electron temperatures  $T_p$ ,  $T_{e,\text{total}}$ .

due to the presence of the current sheet detected already in the raw data with the amplitude  $\delta B/B \simeq 1.4$ . The shape of  $\delta B_1$  (red line) around  $t_0$  is due to the bandpass filtering or a current sheet

shown above in panel (a). The corresponding polarization (panel (f)) is nearly linear. In the legend, we indicate the angles between the corresponding mean field  $\mathbf{B}_0$  and the MVA basis.

The MVA basis vectors  $\mathbf{e}_1$ ,  $\mathbf{e}_2$ , and  $\mathbf{e}_3$  are well defined if both eigenvalue ratios are small,  $\lambda_2/\lambda_1 < 0.3$  and  $\lambda_3/\lambda_2 < 0.3$  (Paschmann & Daly 1998). If only the first (second) of the ratios is below 0.3, then only  $\mathbf{e}_1$  ( $\mathbf{e}_3$ ) is unambiguously defined. The angles with eigenvalue ratios below 0.3 are shown in bold in the legend of the polarization plane. So, one can see a linear polarization, with the maximum variance direction  $\mathbf{e}_1$  quasi-perpendicular to  $\mathbf{B}_0$ ,  $\Theta_{B,1} = 80^\circ$ . The intermediate  $\mathbf{e}_2$  and minimum  $\mathbf{e}_3$  variance directions are ill defined.

Figure 11(c) shows a zoom-in to the time interval of  $\pm 1$  s around the same central time  $t_0$ . The gray horizontal band indicates  $\pm 2\sigma_{\text{ion}}$ . For ion scales, the amplitude is significant,  $\delta\mathbf{B}_{\text{ion}}/B_0 \sim 0.2$ . The shape of  $\delta\mathbf{B}_{\text{ion}}$  is not the filtering remnant of the current sheet, as shown in the Appendix C. The black dashed line shows the fluctuations of magnetic field modulus  $\delta|\mathbf{B}|$ , which are negligible. Here, the local MVA frame is well defined. The minimum and maximum variation directions are perpendicular to the magnetic field. The elliptic polarization and the shape of magnetic fluctuations at ion scales resemble the crossing of a dipole vortex (shown in Figure 6(b)). Thus, we observe a vortex-like structure at ion scales embedded in the current sheet at MHD scales.

Figure 11(d) shows the zoom-in to the time interval of  $\pm 0.07$  s around  $t_0$ . High-amplitude fluctuations  $\delta\mathbf{B}_{\text{sub-ion}}$  with respect to the noise level  $\pm 2\sigma_{\text{sub-ion}}$  (gray band) are well localized in time. The modulus of the magnetic field is fluctuating with a significant amplitude  $\delta|\mathbf{B}|/\delta B_1 = 0.4$  (black dashed line), so the fluctuations are compressible. This is in agreement with a statistical increase of compressibility at the sub-ion range (see the spectrum of compressible fluctuations in Figure 2(b)). The polarization is elliptic; see panel (h). The maximum MVA eigenvector is quasi-perpendicular to the background magnetic field  $\theta_{B_0,1} = 69^\circ$ . These properties can be explained as the crossing of the compressible vortex through its center (Jovanović et al. 2020).

Figures 11(i)–(k) show the magnetic field fluctuations normalized by the background magnetic field  $(\mathbf{B} - \langle \mathbf{B} \rangle)/B_0$ , where  $B_0 = \langle |\mathbf{B}| \rangle_{t-t_0 \in (-100, 100)\text{s}} = 100$  nT, and the proton velocity fluctuations  $(\mathbf{V} - \langle \mathbf{V} \rangle)/V_A$  normalized by the average Alfvén velocity  $V_A = B_0/\sqrt{\mu_0 N_e m_p} = 104$  km s $^{-1}$ . Both  $(\mathbf{B} - \langle \mathbf{B} \rangle)/B_0$  and  $(\mathbf{V} - \langle \mathbf{V} \rangle)/V_A$  are shown in the magnetic field MVA reference frame calculated using the  $(\mathbf{B} - \langle \mathbf{B} \rangle)$  vector over the 200 s shown. Magnetic field and velocity variations across the sheet ( $\Delta$ ) make the angle of  $\alpha(\Delta\mathbf{B}, \Delta\mathbf{V}) = 21^\circ$ . Variations in  $(\mathbf{B} - \langle \mathbf{B} \rangle)/B_0$  and  $(\mathbf{V} - \langle \mathbf{V} \rangle)/V_A$  correlate, but the amplitudes are different  $(|\Delta\mathbf{V}|/V_A)_1 = 0.4 \cdot (|\Delta\mathbf{B}|/B_0)_1$ . Thus, the discontinuity does not fulfill the Walen relation  $\Delta\mathbf{V} = \pm \Delta\mathbf{B}/\sqrt{4\pi\rho}$  for rotational discontinuities. In the presence of pressure anisotropy, the density can change across the discontinuity, and the Walen relation is modified as follows (Hudson 1970; Neugebauer 2006):

$$\begin{aligned} \Delta(A\rho) &= 0 \\ \Delta\mathbf{V} &= (\rho/\mu_0)^{1/2} A^{1/2} \Delta(\mathbf{B}/\rho) \end{aligned} \quad (\text{B1})$$

where  $A = 1 - \mu_0(p_{\parallel} - p_{\perp})/B^2$  is the anisotropy parameter. In the considered time interval  $\beta_p < 0.5$ , so  $A = 1 - 4\pi(p_{\parallel} - p_{\perp})/B^2 > 1 - \beta \sim 0.5$  implies  $A^{1/2} > 0.7$ . However, we would need  $A^{1/2} \sim 0.4$  to explain the observed relationship between  $\Delta\mathbf{V}$  and  $\Delta(\mathbf{B}/\rho)$  with anisotropy.

In Figures 11(l)–(n) we see how the magnetic field modulus  $|\mathbf{B}|$ , velocity modulus  $|\mathbf{V}|$ , electron density  $N_e$ , and ion  $T_i$  and

electron  $T_e$  temperatures change across the structure. Velocity and temperatures stay nearly constant. At the same time,  $|\mathbf{B}|$  and  $N_e$  are anticorrelated: while the magnetic field increases by  $\Delta|\mathbf{B}| = 10$  nT, density decreases by  $\Delta N_e \sim 50$  cm $^{-3}$ . This is usually observed for convected structures in pressure balance. The observed properties are typical for a tangential discontinuity, where magnetic field and density are not constant across the discontinuity.

Another property that distinguishes between RDs and TDs is the magnitude of the normal magnetic field component  $B_n$ . The divergence-free condition implies that  $B_n$  must be constant in the case of planar geometry. So, MVA minimum variance direction should represent normal to the magnetic sheet, and  $B_3 = B_n = \text{constant}$ . Next, tangential discontinuities have  $B_n = 0$ , but in observations  $B_3 \simeq 70$  nT. These results are obtained in the known limits of MVA since the MVA estimation of the normal to the sheet can differ from the normal estimated from multispacecraft methods (Horbury et al. 2001; Knetter et al. 2004).

So, to summarize, starting from the largest-observed scales and up to the end of the inertial range, we observe a current sheet that can be interpreted as a tangential discontinuity (TD). Ion and sub-ion scale substructures are embedded in this discontinuity. The ion scale structure resembles the dipole Alfvén vortex model (see Section 5 and Figure 11 column (b)). The sub-ion scale structure might represent a compressible vortex (Jovanović et al. 2020). A sketch describing this event is given in Figure 8(a).

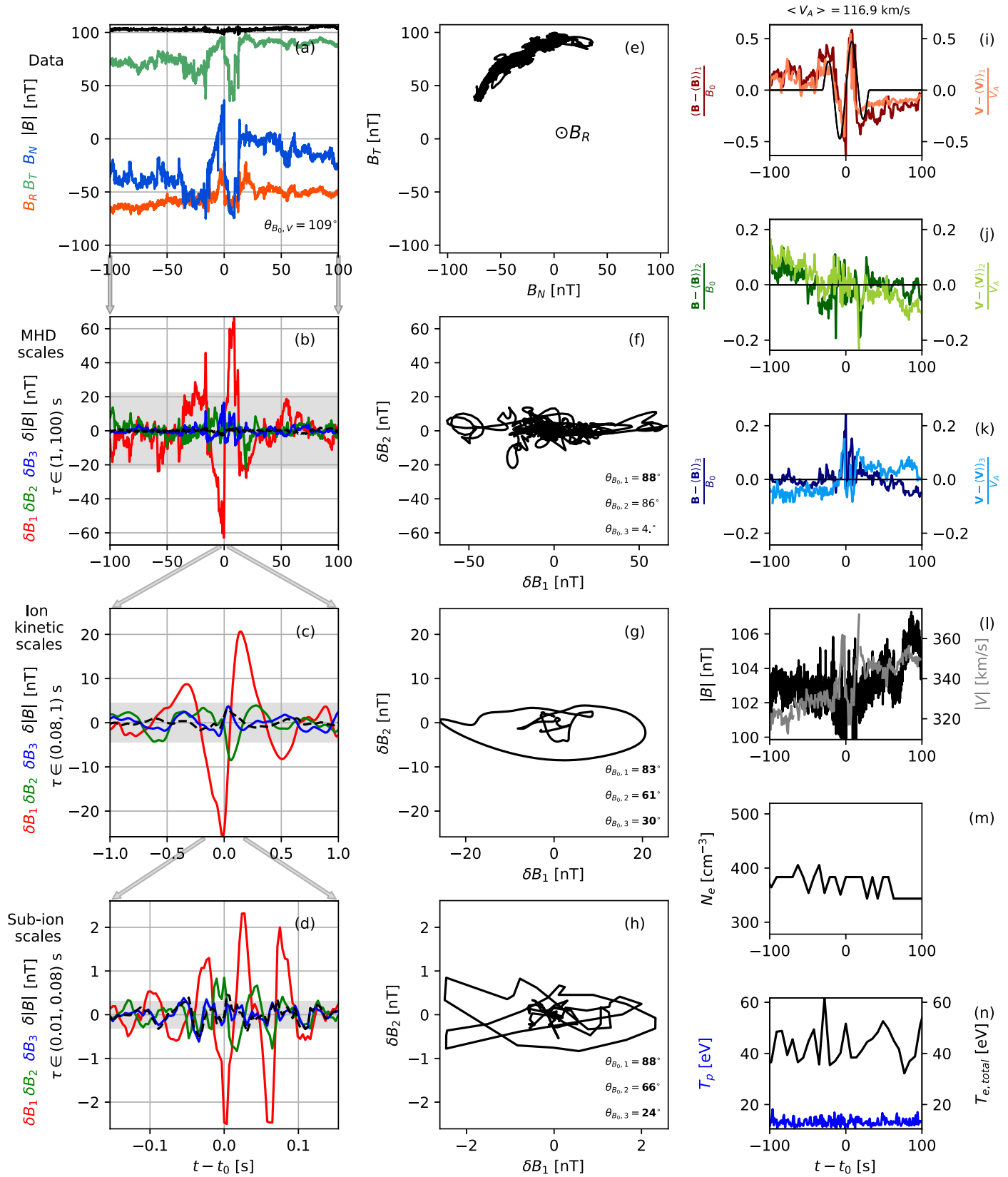
## B.2. Example 2

The second example is shown in Figure 12 in the same format as the first event in Figure 11. The central time of the event is 01:19:20 UT. In panel (a), the raw magnetic field is shown in the RTN reference frame.

Panel (e) shows the polarization  $B_T(B_N)$ ; out-of-plane  $B_R$  does not change sign (this structure is not a switchback). The magnetic field deflects twice within the timescale of  $\sim 80$  s. The magnetic field before crossing the structure and after is oriented differently: it is rotated by  $\Delta\zeta = 15^\circ$  (see Equation (A3)). This can be due to a weak  $(|\Delta\mathbf{B}|/B_0 = (\mathbf{B}_{t=-100\text{s}} - \mathbf{B}_{t=100\text{s}})/B_0 \simeq 0.3)$  rotational current sheet, since the ratio of velocity and magnetic field jumps satisfies the Walen relation  $|\Delta\mathbf{V}|/V_A = 1.03 \cdot |\Delta\mathbf{B}|/B_0$ .

Magnetic fluctuations at the MHD scales  $\delta\mathbf{B}_{\text{MHD}}$  are shown in Figure 12(b) in the MVA reference frame. The amplitude of the structure  $\delta B_1 \simeq 60$  nT (i.e., from peak to peak  $\Delta B/B_0 \sim 1.2$ ) well exceeds the level of incoherent signal  $2\sigma_{\text{MHD}} = 22$  nT. The direction of the maximum eigenvector  $\mathbf{e}_1$  is well distinguished from intermediate ( $\mathbf{e}_2$ ) and minimum ( $\mathbf{e}_3$ ) directions since  $\lambda_2/\lambda_1 = 0.06$ , and it is perpendicular to the background magnetic field  $\theta_{B_0,1} = 88^\circ$ .

The velocity and magnetic field fluctuations are well correlated,  $\delta B/B_0 = \xi \delta V/V_A$ ; see panels (i)–(k). The proportionality coefficient is  $\xi = 0.86$  for magnetic fluctuations at MHD scales and  $\xi = 0.81$  in the raw data with the mean value subtracted for the same time interval. The black lines in panels (i)–(k) show the fluctuations of the monopole Alfvén vortex model, along the central crossing. The observed time profiles of fluctuations agree well with the Alfvén vortex model. The magnetic field vector before and after the vortex crossing is oriented differently:  $|\mathbf{B}(t_0 - 70\text{s}) - \mathbf{B}(t_0 + 70\text{s})|/B_0 = (0.4, 0.03, 0.03)$ ; (in the MVA reference frame). Thus, the vortex is embedded in a relatively weak current sheet.

$t_0 = 1:19:20$ 


**Figure 12.** Example 2: an Alfvén vortex embedded in a weak current sheet on MHD scales. The format is the same as in Figure 11.

In the plasma rest frame, this vortex propagates with a negligible speed of  $\simeq 3 \text{ km s}^{-1}$  (see the main text of the paper), so the Taylor hypothesis can be used to estimate its spatial scale. PSP trajectory crosses the structure in a plane nearly perpendicular to  $\mathbf{B}_0$  ( $\theta_{B_0, V} = 71^\circ$ ). The diameter of the vortex can be estimated as  $d = \theta_{B_0, V} \cdot V \Delta t \sim 2.4 \times 10^4 \text{ km}$ . Given that the mean ion inertial length is  $d_i \simeq 11 \text{ km}$  and the mean ion Larmor radius is  $\rho_i = 5 \text{ km}$ , the vortex diameter  $d \simeq 2 \times 10^3 d_i = 5 \times 10^3 \rho_i$ . The variation of the magnetic field modulus is negligible,  $\delta|\mathbf{B}|/B_0 = 0.03$ , as are the variations of  $N_e$ ,  $T_e$ , and  $T_p$ ; see panels (l)–(n). The change of  $|\mathbf{V}|$  (gray line in panel (l)) is due to the superposition of the velocity fluctuation of the Alfvén vortex on the bulk solar wind speed.

Figure 12(c) shows the ion scale magnetic fluctuations  $\delta\mathbf{B}_{\text{ion}}$  located in the center of the MHD scale Alfvén vortex. The maximum amplitude of the fluctuation,  $\max(|\delta B_i|) = 24 \text{ nT}$ , as well as two secondary peaks on the left and right sides exceed well the incoherent threshold  $\pm 2\sigma_{\text{ion-scale}}$  shown in gray. The polarization is elliptical (panel (g)), and the maximum variance is perpendicular to the local field direction. These observed properties are in agreement with an Alfvén vortex crossing with a finite impact distance from its center. The vortex was observed during  $\Delta t = 1.5 \text{ s}$ . The diameter of the vortex is  $d = V \Delta t \sin(\Theta_{BV}) = 440 \text{ km} = 40d_i = 90\rho_i$ , where  $\Delta t = 1.5 \text{ s}$  is the crossing duration,  $V = 330 \text{ km s}^{-1}$ ,  $\Theta_{BV} = 70^\circ$ ,  $d_i = 11 \text{ km}$ , and  $\rho_i = 5 \text{ km}$ .

Figure 12(d) shows the sub-ion fluctuations  $\delta\mathbf{B}_{\text{sub-ion}}$ , which are 10 times more intense than the incoherent threshold. They are quasi-transverse,  $\theta_{B_0, 1} = 88^\circ$  and  $\theta_{B_0, 2} = 64^\circ$ , and weakly compressible,  $\max(\delta B_i) \approx \max(\delta B_3) < 0.2 \max(\delta B_1)$ . The polarization is elliptical. The maximum variance is perpendicular to the local field, as in the case of ion and MHD scale structures. The crossing duration is  $\Delta t \simeq 0.15 \text{ s}$ ; i.e., the cross-section scale is about 47 km, or  $4d_i$  or  $9\rho_i$ . The fluctuations can be explained by the compressible Alfvén vortex model (Jovanović et al. 2020).

In summary, in the example of Figure 12, in raw data we observe a weak current sheet with the thickness of the high-amplitude MHD scale structure embedded in it. This current sheet is Alfvénic in nature, which is the property of a rotational discontinuity. We can interpret the MHD structure embedded in the weak rotational current sheet as a monopole Alfvén vortex crossed close to its center. Within this monopole Alfvén vortex, we observe smaller vortices at ion and sub-ion scales. Figure 8(b) shows the sketch of the Example 2.

### B.3. Example 3

Figure 13 shows an example observed at around  $t_0 = 2:19:38 \text{ UT}$ . In panel (a), the center of the current sheet is observed at  $t - t_0 = 20 \text{ s}$ , when the magnetic field rotates by the angle  $\Delta\zeta = 110^\circ$ .  $B_R$  changes sign across the sheet, so the sheet forms the boundary of a switchback, similar to observations in Krasnoselskikh et al. (2020).

Figure 13(b) shows MHD scale fluctuations in the MVA reference frame. The amplitude of fluctuations associated with the discontinuity exceeds the level of the incoherent signal (see the gray horizontal band). Panels (e)–(f) show the corresponding polarizations.

The fluctuations are nearly Alfvénic in the vicinity of the discontinuity:  $(\mathbf{B} - \langle \mathbf{B} \rangle)_1 / B_0 = 1.25 \cdot (\mathbf{V} - \langle \mathbf{V} \rangle)_1 / V_A$ , when  $t - t_0 \in (0, 40) \text{ s}$ ; see Figures 13(i)–(k). But further away from the discontinuity  $\Delta B/B_0$  and  $\Delta V/V_A$  have different

amplitudes:  $\Delta B_1/B_0 \approx 2.2 \cdot \Delta V_1/V_A$ , where  $\Delta B_1 = |B_1(t_0 - 100 \text{ s}) - B_1(t_0 + 100 \text{ s})|$  and  $\Delta V_1 = |V_1(t_0 - 100 \text{ s}) - V_1(t_0 + 100 \text{ s})|$ . The magnetic field modulus decreases from 105 nT at the boundaries to 90 nT in the center (panel (l)). The duration of this magnetic cavity is  $\Delta t \simeq 100 \text{ s}$ , which corresponds to the scale of  $l = \Delta t \cdot V = 3.5 \times 10^4 \text{ km} = 3 \times 10^3 d_i = 5 \times 10^3 \rho_i$ . The density  $N_e$ , Figure 13(m), weakly increases across the discontinuity. The proton temperature  $T_p$ , Figure 13(n), is higher on the left side of the discontinuity than on the right; it has a local maximum around the discontinuity center in contrast to a nearly uniform  $T_e$ . There is an anticorrelation between the magnetic field modulus and plasma density  $N_e$ , indicating a possible pressure balance. The polarization of magnetic fluctuations is arch like, which is typical for rotational discontinuities (Tsurutani et al. 1996; Sonnerup et al. 2010; Haaland et al. 2012; Paschmann et al. 2013).

Magnetic fluctuations at ion scales are shown in Figure 13(c). The maximum and intermediate magnetic fluctuations ( $\delta B_1$  and  $\delta B_2$ ) are transverse and have nearly the same amplitude; the polarization is close to elliptical (Figure 13(g)). The described properties (i.e., localized transverse fluctuations with nearly elliptical polarization) are consistent with the off-center monopole Alfvén vortex crossing; see Figure 6(a). The minimum MVA eigenvector  $\mathbf{e}_3$  is well defined, because  $\lambda_3/\lambda_2 = 0.06$  is small. From the model crossings (see Section 5.1.1) we know that if the spacecraft is crossing the monopole Alfvén vortex,  $\mathbf{e}_3$  is a good approximation for the axis of the vortex. We can conclude that the axis of the vortex is nearly parallel to the background magnetic field, since  $\theta_{B_0, 3} = 8^\circ$ .

The sub-ion scale structure, Figure 13(d), is well localized in time and has a significantly compressible component,  $\delta|\mathbf{B}| \sim 0.5 \delta B_1$ . This high compressibility is a typical property of structures at these scales. Such localized compressible magnetic fluctuations at sub-ion scales can be interpreted as the compressible Alfvén vortex (Jovanović et al. 2020).

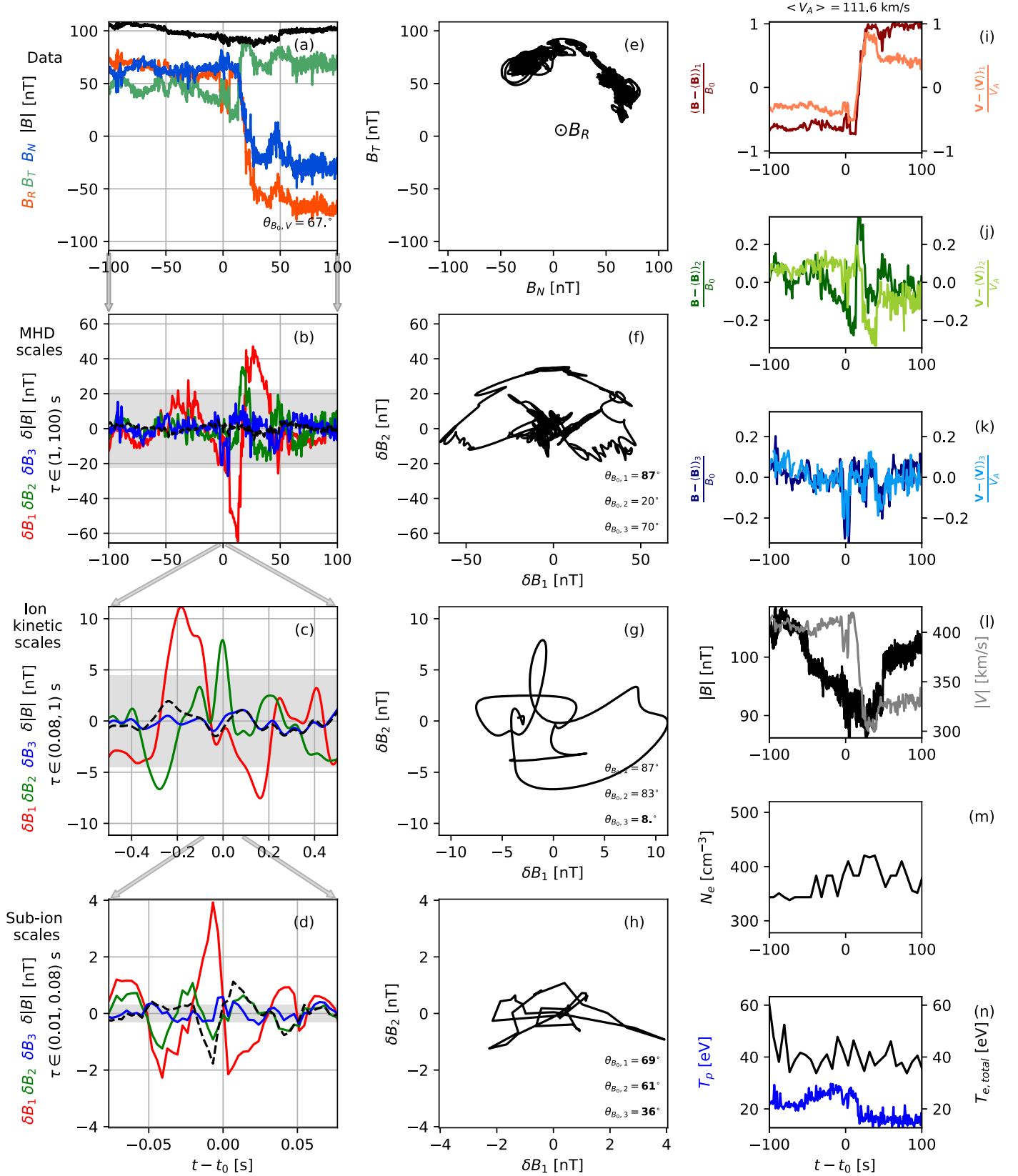
### B.4. Example 4

Figure 14 shows the details of the fourth example. In panel (a) the radial magnetic field  $B_R$  is positive in two time intervals:  $t - t_0 \in (-30, 0) \text{ s}$  and  $t - t_0 \in (25, 80) \text{ s}$ . These are two neighboring switchbacks. The crossing is nearly perpendicular to the mean background magnetic field  $\mathbf{B}_0$  ( $\theta_{BV} = 71^\circ$ ), since  $\mathbf{B}_0 = \langle \mathbf{B} \rangle_{t-t_0 \in (-100, 100) \text{ s}} = (11, 84, -14) \text{ nT}$  is directed mainly along the tangential direction in the RTN reference frame, and the solar wind bulk speed is  $\mathbf{V} = \langle \mathbf{V} \rangle_{t-t_0 \in (-100, 100) \text{ s}} = (400, 80, 0) \text{ km s}^{-1}$ .

Figure 14(b) shows the MHD scale bandpass-filtered magnetic fluctuations in the MVA reference frame. We observe sharp discontinuities at the boundaries of both neighboring switchbacks. The magnetic field and velocity fluctuations are well correlated, and the normalized amplitudes of  $\mathbf{B} - \langle \mathbf{B} \rangle / B_0$  and  $\mathbf{V} - \langle \mathbf{V} \rangle / V_A$  are equal (see panels (i)–(k)), so the fluctuations are Alfvénic. The density  $N_e$  is constant across the structure; see panel (m). The proton temperature  $T_p$  is increased by  $\sim 30\%$  in both neighboring switchbacks compared to the value outside; see panel (n).

Similar to the previous examples, the embedded structures are observed near the central time of the event  $t - t_0 = 0 \text{ s}$  (at the right boundary of the first switchback). Fluctuations of ion scales are shown in panel (c). The polarization is close to linear; see panel (g). The maximum variance direction is perpendicular

$t_0 = 2:19:38$



**Figure 13.** Example 3: a rotational discontinuity (switchback boundary) nested in a larger magnetic depression region on MHD scales. The format is the same as in Figure 11.

$t_0 = 2:54:08$

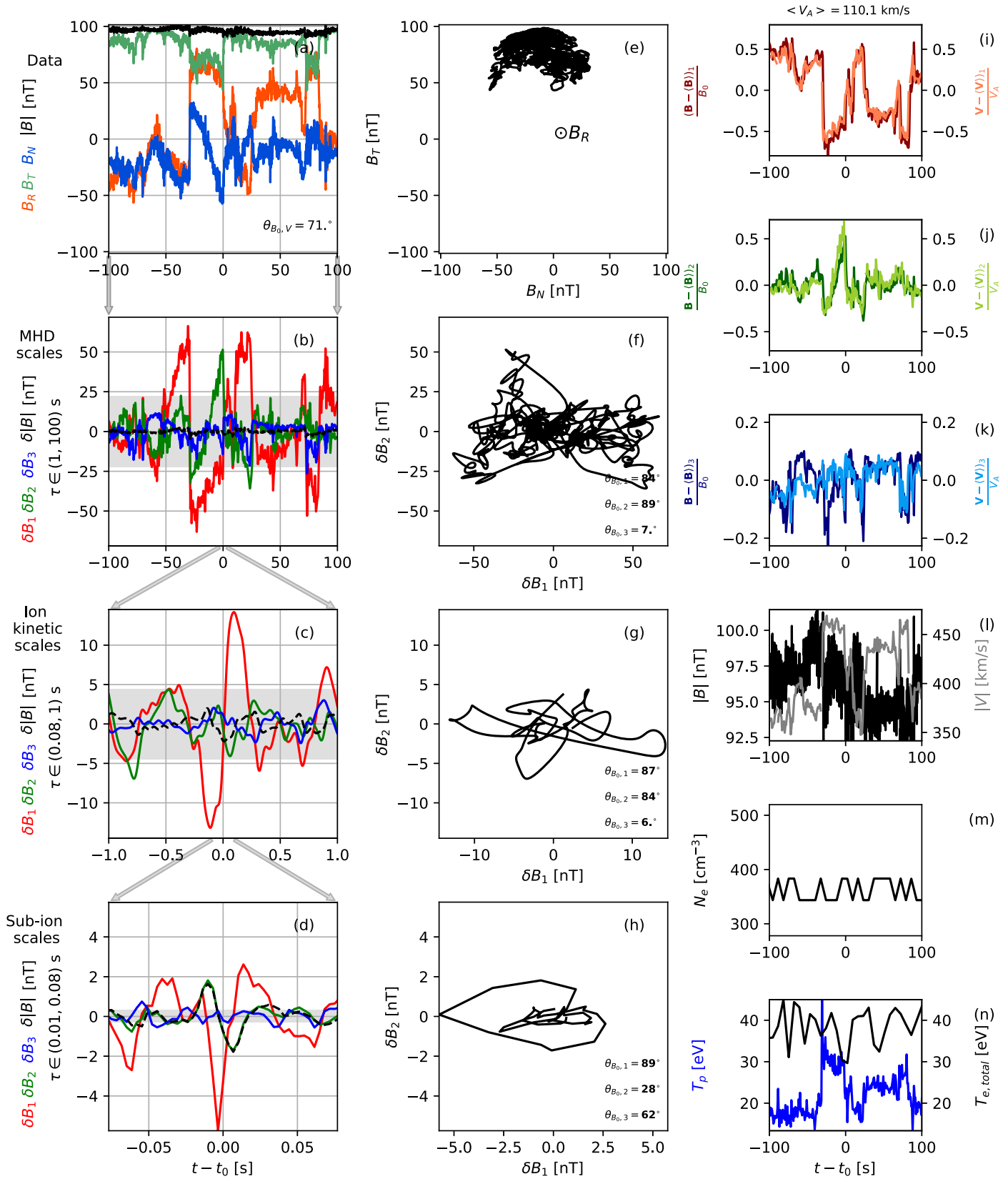


Figure 14. Example 4: two neighboring switchback structures. The format is the same as in Figure 11.

to the local background magnetic field. The time profile of the corresponding component  $\delta B_1$  is consistent with the monopole Alfvén vortex crossing through the center.

Figure 14(d) shows the sub-ion fluctuations. The profile of the maximum variance component  $\delta B_1$  has a peak. The intermediate component  $\delta B_2$  coincides with  $\delta|B|$ , so the structure is compressible, with  $\delta|B|/\max|\delta B_1| \sim 0.3$ . We interpret this structure as a compressible ion scale vortex (Jovanović et al. 2020).

### B.5. Summary of Detected Structures

We collected large statistics of coherent structures (Figure 4). Some of these events at MHD scales represent isolated current sheets such as tangential and rotational current sheets; see two examples shown in Appendices B.1 and B.3, respectively. However, we found that current sheets are rare, and most of the events can be interpreted as Alfvén vortices. The example in Appendix B.2 (Figure 12) is interpreted as the crossing of a monopole vortex along its center (embedded in a weak and large-scale rotational discontinuity). From the visual examination of  $\sim 200$  events, we find that the embedded structures at ion and sub-ion scales are mostly Alfvén vortices, independent of the existence of a CS at large scales. From the examples shown here, in the case of CS at large scales, the sub-ion vortices are compressible, and, in the case of the large-scale Alfvén vortex, the small-scale vortex is incompressible.

## Appendix C Necessity of Bandpass Filtering

At ion and sub-ion scales the amplitude of embedded substructures is much smaller than the amplitude of MHD scale fluctuations and the background magnetic field. Therefore, filtration allows to remove the quasi-constant background, which facilitates the analysis of the fluctuations associated with substructures. However, the filtration may introduce an ambiguity in the interpretation of the signal. Let us consider the thin (i.e.,  $\ell \sim d_i$ ) current sheet, so that the crossing duration is  $\Delta t = 0.125$  s. Figure 15 shows the tangential magnetic field component of the current sheet (blue) and the result of the filtration (orange).

In Figure 15(a) the filter frequency window corresponds to the MHD inertial range, as defined in Section 3 in Equation (6). Since the thickness of the sheet is small,  $\Delta t/\min(\tau_{\text{MHD}}) = 0.1$ , the filtered signal has a steep jump of the same amplitude as the amplitude of the initial signal. However, unlike the initial signal, the filtered signal tends to 0 at the scale  $|t| > \max(\tau_{\text{MHD}})/2$  away from the discontinuity. Two low-amplitude local extremes appear at  $t = \pm 50$  s.

Figure 15(b) shows the result of the filtration at ion scales. The magnetic field changes sign smoothly. If the thickness of an intense coherent structure is smaller than the minimum timescale of the MHD range, and if the classification method is based on the shape of the most intense filtered magnetic field component, then the CS filtration remnant at ion scales can be misclassified as an embedded monopole Alfvén vortex crossed through its center.

In conclusion, filtering is necessary for the study of ion and sub-ion scale structures because such structures have small amplitude compared to  $B_0$ , and they are poorly distinguishable in raw data. However, filtering can significantly change the

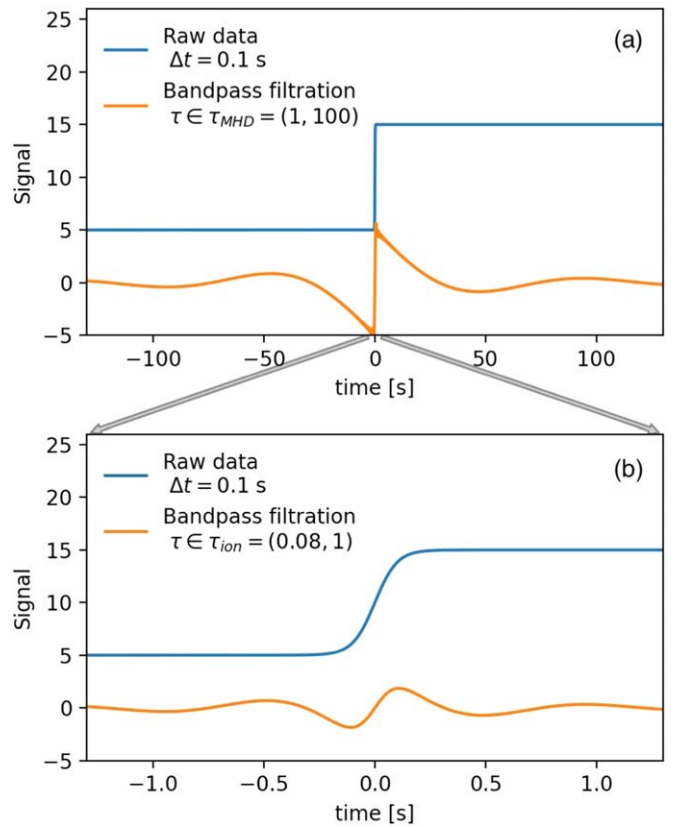


**Figure 15.** Filtration of the current sheet. The temporal scale of the current sheet is  $\Delta t = 0.1$  s. The top panel (a) shows the raw data (blue line) and the bandpass-filtered signal at the MHD range of timescales  $\tau \in \tau_{\text{MHD}}$  (orange). The bottom panel shows the zoom-in to the shorter time interval. The same raw data as in panel (a) are shown in blue. The orange line in panel (b) shows the bandpass filtration at  $\tau \in \tau_{\text{ion}}$ .

waveform, which complicates the direct comparison of structures with models. For example, the current sheet does not look like a step function after filtering. However, signal filtering has little effect on the polarization of fluctuations. For example, if the spacecraft is crossing a tangential discontinuity (see Equation (A4)) with only one component of the magnetic field changed, i.e., with linear polarization, then after filtering the shape of the signal will change, but the polarization will remain linear. Suppose the spacecraft is crossing an Alfvén vortex and the measured polarization is close to elliptical in raw data. In that case, filtering will remove the quasi-constant background magnetic field, but the polarization will remain elliptical. The polarization is convenient to show the amplitude anisotropy of a 2D vector. But in the general case the magnetic fluctuations are a 3D vector. So, the amplitude anisotropy can be characterized by MVA eigenvalue relations.

### ORCID iDs

Alexander Vinogradov <https://orcid.org/0000-0002-4355-3022>

Olga Alexandrova <https://orcid.org/0000-0003-3811-2991>

Pascal Démoulin <https://orcid.org/0000-0001-8215-6532>

Anton Artemyev <https://orcid.org/0000-0001-8823-4474>

Milan Maksimovic <https://orcid.org/0000-0001-6172-5062>

Alexei Vasiliev <https://orcid.org/0000-0002-2008-7647>

Stuart Bale <https://orcid.org/0000-0002-1989-3596>



## References

- Alexandrova, O. 2008, *NPGeo*, **15**, 95
- Alexandrova, O. 2020, PhD thesis, Observatoire de Paris, Université Paris Sciences et Lettres (PSL), <https://hal.science/tel-03999422>
- Alexandrova, O., Chen, C. H. K., Sorriso-Valvo, L., Horbury, T. S., & Bale, S. D. 2013, *SSRv*, **178**, 101
- Alexandrova, O., Jagarlamudi, V. K., Hellinger, P., et al. 2021, *PhRvE*, **103**, 063202
- Alexandrova, O., Krishna Jagarlamudi, V., Rossi, C., et al. 2020, arXiv:2004.01102
- Alexandrova, O., Lacombe, C., Mangeney, A., Grappin, R., & Maksimovic, M. 2012, *ApJ*, **760**, L21
- Alexandrova, O., Mangeney, A., Maksimovic, M., et al. 2006, *JGRA*, **111**, A12208
- Alexandrova, O., & Saur, J. 2008, *GeoRL*, **35**, L15102
- Alexandrova, O., Saur, J., Lacombe, C., et al. 2009, *PhRvL*, **103**, 165003
- Alterman, B. L., & Kasper, J. C. 2019, *ApJL*, **879**, L6
- Artemyev, A. V., Angelopoulos, V., & Vasko, I. Y. 2019, *JGRA*, **124**, 3858
- Bale, S. D., Badman, S. T., Bonnell, J. W., et al. 2019, *Natur*, **576**, 237
- Bale, S. D., Goetz, K., Harvey, P. R., et al. 2016, *SSRv*, **204**, 49
- Baumjohann, W., & Treumann, R. A. 1997, *Basic Space Plasma Physics* (London: Imperial College Press)
- Borovsky, J. E. 2008, *JGRA*, **113**, A08110
- Bowen, T. A., Bale, S. D., Bonnell, J. W., et al. 2020, *JGRA*, **125**, e27813
- Bruno, R. 2019, *E&SS*, **6**, 656
- Bruno, R., Carbone, V., Veltri, P., Pietropaolo, E., & Bavassano, B. 2001, *P&SS*, **49**, 1201
- Burlaga, L. F. 1969, *SoPh*, **7**, 54
- Chasapis, A., Retinò, A., Sahraoui, F., et al. 2015, *ApJL*, **804**, L1
- Chen, C. H. K., Bale, S. D., Bonnell, J. W., et al. 2020, *ApJS*, **246**, 53
- Chen, C. H. K., Horbury, T. S., Schekochihin, A. A., et al. 2010, *PhRvL*, **104**, 255002
- Eastwood, J. P., Stawarz, J. E., Phan, T. D., et al. 2021, *A&A*, **656**, A27
- Farge, M. 1992, *AnRFM*, **24**, 395
- Farge, M., & Schneider, K. 2015, *JPIPh*, **81**, 435810602
- Feng, H. Q., Wu, D. J., Lin, C. C., et al. 2008, *JGRA*, **113**, A12105
- Fiedler, H. E. 1988, *PrAes*, **25**, 231
- Goodrich, C. C., & Cargill, P. J. 1991, *GeoRL*, **18**, 65
- Greco, A., Chuychai, P., Matthaeus, W. H., Servidio, S., & Dmitruk, P. 2008, *GeoRL*, **35**, L19111
- Greco, A., Matthaeus, W. H., D'Amicis, R., Servidio, S., & Dmitruk, P. 2012, *ApJ*, **749**, 105
- Greco, A., Matthaeus, W. H., Perri, S., et al. 2018, *SSRv*, **214**, 1
- Greco, A., Matthaeus, W. H., Servidio, S., Chuychai, P., & Dmitruk, P. 2009, *ApJL*, **691**, L111
- Greco, A., Perri, S., Servidio, S., Yordanova, E., & Veltri, P. 2016, *ApJL*, **823**, L39
- Haaland, S., Sonnerup, B., & Paschmann, G. 2012, *AnGeo*, **30**, 867
- Hada, T., Koga, D., & Yamamoto, E. 2003, *SSRv*, **107**, 463
- Harris, E. G. 1962, *NCim*, **23**, 115
- Haynes, C. T., Burgess, D., Camporeale, E., & Sundberg, T. 2015, *PhPI*, **22**, 012309
- Horbury, T. S., Burgess, D., Fränz, M., & Owen, C. J. 2001, *GeoRL*, **28**, 677
- Hudson, P. D. 1970, *P&SS*, **18**, 1611
- Hussain, A. K. M. F. 1986, *JFM*, **173**, 303
- Janvier, M., Démoulin, P., & Dasso, S. 2014, *SoPh*, **289**, 2633
- Jovanović, D., Alexandrova, O., Maksimović, M., & Belić, M. 2018, *JPIPh*, **84**, 725840402
- Jovanović, D., Alexandrova, O., Maksimović, M., & Belić, M. 2020, *ApJ*, **896**, 8
- Kadomtsev, B. B., & Pogutse, O. P. 1974, *JETP*, **38**, 283
- Karimabadi, H., Roytershteyn, V., Wan, M., et al. 2013, *PhPI*, **20**, 012303
- Kasper, J. C., Abiad, R., Austin, G., et al. 2016, *SSRv*, **204**, 131
- Kasper, J. C., Bale, S. D., Belcher, J. W., et al. 2019, *Natur*, **576**, 228
- Kasper, J. C., Stevens, M. L., Lazarus, A. J., Steinberg, J. T., & Ogilvie, K. W. 2007, *ApJ*, **660**, 901
- Kiyani, K. H., Osman, K. T., & Chapman, S. C. 2015, *RSPTA*, **373**, 20140155
- Knetter, T., Neubauer, F. M., Horbury, T., & Balogh, A. 2004, *JGRA*, **109**, A06102
- Koga, D., & Hada, T. 2003, *SSRv*, **107**, 495
- Krasnoselskikh, V., Larosa, A., Agapitov, O., et al. 2020, *ApJ*, **893**, 93
- Kuzay, D., Alexandrova, O., & Matteini, L. 2019, *PhRvE*, **99**, 053202
- Lacombe, C., Alexandrova, O., & Matteini, L. 2017, *ApJ*, **848**, 45
- Li, G., Miao, B., Hu, Q., & Qin, G. 2011, *PhRvL*, **106**, 125001
- Lion, S., Alexandrova, O., & Zaslavsky, A. 2016, *ApJ*, **824**, 47
- Liu, M., Issautier, K., Meyer-Vernet, N., et al. 2021, *A&A*, **650**, A14
- Lotekar, A. B., Vasko, I. Y., Phan, T., et al. 2022, *ApJ*, **929**, 58
- Mangeney, A. 2001, in *ESA Special Publication*, Vol. 492, *Sheffield Space Plasma Meeting: Multipoint Measurements versus Theory*, ed. B. Warmbein (Noordwijk: ESA), 53
- Matteini, L., Franci, L., Alexandrova, O., et al. 2020, *FrASS*, **7**, 83
- Meyrand, R., Squire, J., Mallet, A., & Chandran, B. D. G. 2023, arXiv:2308.10389
- Moldwin, M. B., Ford, S., Lepping, R., Slavin, J., & Szabo, A. 2000, *GeoRL*, **27**, 57
- Moncuquet, M., Meyer-Vernet, N., Issautier, K., et al. 2020, *ApJS*, **246**, 44
- Neugebauer, M. 1989, *GeoRL*, **16**, 1261
- Neugebauer, M. 2006, *JGRA*, **111**, A04103
- Osman, K. T., Matthaeus, W. H., Greco, A., & Servidio, S. 2011, *ApJL*, **727**, L11
- Papini, E., Cicone, A., Franci, L., et al. 2021, *ApJL*, **917**, L12
- Paschmann, G., & Daly, P. W. 1998, in *Analysis Methods for Multi-Spacecraft Data*. ISSI Scientific Reports Ser., ESA/ISSI, Vol. 1, ed. G. Paschmann & P. Daly (Noordwijk: ESA)
- Paschmann, G., Haaland, S., Sonnerup, B., & Knetter, T. 2013, *AnGeo*, **31**, 871
- Perrone, D., Alexandrova, O., Mangeney, A., et al. 2016, *ApJ*, **826**, 196
- Perrone, D., Alexandrova, O., Roberts, O. W., et al. 2017, *ApJ*, **849**, 49
- Perrone, D., Bruno, R., D'Amicis, R., et al. 2020, *ApJ*, **905**, 142
- Petviashvili, V., & Pokhotelov, O. 1992, *Solitary Waves in Plasmas and in the Atmosphere* (Philadelphia, PA: Gordon and Breach)
- Riley, P., Sonett, C. P., Tsurutani, B. T., et al. 1996, *JGR*, **101**, 19987
- Roberts, O. W., Li, X., Alexandrova, O., & Li, B. 2016, *JGRA*, **121**, 3870
- Roytershteyn, V., Karimabadi, H., & Roberts, A. 2015, *RSPTA*, **373**, 20140151
- Salem, C. 2000, PhD thesis, Univ. Paris
- Salem, C., Mangeney, A., Bale, S. D., & Veltri, P. 2009, *ApJ*, **702**, 537
- Salem, C. S., Howes, G. G., Sundkvist, D., et al. 2012, *ApJL*, **745**, L9
- Sonnerup, B. U. Ö., Haaland, S. E., & Paschmann, G. 2010, *AnGeo*, **28**, 1229
- Sonnerup, B. U. Ö., & Scheible, M. 1998, in *Analysis Methods for Multi-Spacecraft Data*. ISSI Scientific Reports Ser., ESA/ISSI, Vol. 1, ed. G. Paschmann & P. Daly (Noordwijk: ESA), 185
- Servidio, S., Matthaeus, W. H., & Dmitruk, P. 2008, *PhRvL*, **100**, 095005
- Sioulas, N., Shi, C., Huang, Z., & Velli, M. 2022, *ApJL*, **935**, L29
- Siscoe, G. L., Davis, L. J., Coleman, P. J. J., Smith, E. J., & Jones, D. E. 1968, *JGR*, **73**, 61
- Smith, S. 1997, *The Scientist and Engineer's Guide to Digital Signal Processing* (1st ed.; San Diego, CA: California Technical Publishing, Inc.)
- Stevens, M. L., & Kasper, J. C. 2007, *JGRA*, **112**, A05109
- Strauss, H. R. 1976, *PhFI*, **19**, 134
- Torrence, C., & Compo, G. P. 1998, *BAMS*, **79**, 61
- Tsurutani, B. T., Ho, C. M., Arballo, J. K., et al. 1996, *JGR*, **101**, 11027
- Tsurutani, B. T., Lakhina, G. S., Verkhoglyadova, O. P., et al. 2011, *JASTP*, **73**, 5
- Turner, J. M., Burlaga, L. F., Ness, N. F., & Lemaire, J. F. 1977, *JGR*, **82**, 1921
- Veltri, P. 1999, *PPCF*, **41**, A787
- Veltri, P., Nigro, G., Malara, F., Carbone, V., & Mangeney, A. 2005, *NPGeo*, **12**, 245
- Verkhoglyadova, O. P., Dasgupta, B., & Tsurutani, B. T. 2003, *NPGeo*, **10**, 335
- Volwerk, M., Goetz, C., Plaschke, F., et al. 2020, *AnGeo*, **38**, 51
- Wan, M., Matthaeus, W. H., Karimabadi, H., et al. 2012, *PhRvL*, **109**, 195001
- Wang, G. Q., Zhang, T. L., Xiao, S. D., et al. 2020, *JGRA*, **125**, e28320
- Wang, R., Vasko, I. Y., Phan, T. D., & Mozer, F. S. 2024, *JGRA*, **129**, e2023JA032215
- Wang, T., Alexandrova, O., Perrone, D., et al. 2019, *ApJL*, **871**, L22
- Wu, P., Perri, S., Osman, K., et al. 2013, *ApJL*, **763**, L30
- Zhao, L. L., Zank, G. P., Adhikari, L., et al. 2020, *ApJS*, **246**, 26
- Zhdankin, V., Boldyrev, S., Mason, J., & Perez, J. C. 2012, *PhRvL*, **108**, 175004
- Zhdankin, V., Uzdensky, D. A., Perez, J. C., & Boldyrev, S. 2013, *ApJ*, **771**, 124